



## Test beam results of a stereo preshower integrated in the liquid argon accordion calorimeter

A. Astbury, B. Aubert, E. Auge, L. Baisin, F. Barreiro, G. Battistoni, A. Bazan, Jm. Baze, G. Beaudoin, B. Beaugiraud, et al.

### ► To cite this version:

A. Astbury, B. Aubert, E. Auge, L. Baisin, F. Barreiro, et al.. Test beam results of a stereo preshower integrated in the liquid argon accordion calorimeter. Nuclear Instruments and Methods in Physics Research Section A: Accelerators, Spectrometers, Detectors and Associated Equipment, Elsevier, 1998, 411, pp.313-329. <in2p3-00000431>

**HAL Id: in2p3-00000431**

**<http://hal.in2p3.fr/in2p3-00000431>**

Submitted on 5 Feb 1999

**HAL** is a multi-disciplinary open access archive for the deposit and dissemination of scientific research documents, whether they are published or not. The documents may come from teaching and research institutions in France or abroad, or from public or private research centers.

L'archive ouverte pluridisciplinaire **HAL**, est destinée au dépôt et à la diffusion de documents scientifiques de niveau recherche, publiés ou non, émanant des établissements d'enseignement et de recherche français ou étrangers, des laboratoires publics ou privés.

# Test beam results of a stereo preshower integrated in the liquid argon accordion calorimeter

The RD3 Collaboration

R.A. Davis, D.M. Gingrich<sup>1</sup>, G.Greenious, P.Kitching, B.Olsen., J.L. Pinfold and N.L. Rodning  
*University of Alberta, Edmonton, Alberta, Canada*

E. Boos and B.O. Zhautykov  
*HEPI, Alma-Ata, Kazakhstan*

B. Aubert, A. Bazan, B. Beaugiraud, J. Boniface, J. Colas, G. Eynard, S. Jézéquel<sup>2</sup>, T. Leflour,  
O. Linossier, S. Nicoleau, G. Sauvage, J. Thion, D. VanDenPlas, I. Wingerter-Seez,  
R. Zitoun and Y.P. Zolnierowski  
*LAPP, Annecy, France*

M. Chmeissani, E. Fernandez, Ll. Garrido, M. Martinez and C. Padilla  
*Univ. Autònoma Barcelona, Bellaterra, Spain*

M. Citterio, H.A. Gordon, D. Lissauer, H. Ma, D. Makowiecki, V. Radeka, D.C. Rahm, S. Rescia,  
D. Stephani and H. Takai  
*Brookhaven National Laboratory, Upton, USA*

L. Baisin, J.C. Berset, J.L. Chevalley, F. Gianotti<sup>3</sup>, O. Gildemeister, C.P. Marin, M. Nessi,  
L. Poggioli, W. Richter and V. Vuillemin  
*CERN, Geneva, Switzerland*

J.M. Baze, E. Delagnes, L. Gosset, P. Lavocat, J.P. Lottin, B. Mansoulié, J.P. Meyer, J.F. Renardy,  
J. Schwindling, S. Simion, J.P. Taguet, J. Teiger and C. Walter  
*CEA, DSM/DAPNIA/SPP, CE Saclay, Gif-sur-Yvette, France*

J. Collot, P. de Saintignon, J.Y. Hostachy, and G. Mahout  
*ISN - IN2P3 / Université Joseph Fourier, Grenoble, France*

F. Barreiro, J. Del Peso, J. Garcia, L. Hervas, L. Labarga, P. Romero, C. Scheel  
*Univ. Autònoma Madrid, Spain*

A. Chekhtman, M.C. Cousinou, P. Dargent, B. Dinkespiller, F. Etienne, P. Fassnacht,  
D. Fouchez, L. Martin, A. Miotto, E. Monnier, E. Nagy, C. Olivetto and S. Tisserant  
*CPP Marseille, France*

G. Battistoni, D.V. Camin, D. Cavalli, G. Costa, L. Cozzi, N. Fedyaikin, A. Ferrari,

---

<sup>1</sup>Also at TRIUMF, Vancouver, B.C., Canada.

<sup>2</sup>Corresponding author, e-mail: jezequel@lapp.in2p3.fr

<sup>3</sup>Also University of Milano, Italy.

L. Mandelli, M. Mazzanti, L. Perini, S. Resconi and P. Sala  
*Dipartimento di Fisica dell'Università e Sezione INFN, Milano, Italy*

G. Beaudoin, P. Depommier, E. León-Florián, C. Leroy and P. Roy  
*University of Montreal, Montreal, Canada*

E. Augé, D. Breton, R. Chase, J.C. Chollet, C. de La Taille, L. Fayard, D. Fournier, J. Gonzales,  
A. Hrisoho, Y. Jacquier, B. Merkel, I. Nikolic, J.M. Noppe, G. Parrou, P. Petroff, P. Puzo,  
J.P. Richer, A. Schaffer, N. Seguin-Moreau, L. Serin, V. Tisserand, J.J. Veillet and I. Vichou  
*LAL, Orsay, France*

B. Canton, J. David, J.F. Genat, D. Imbault, O. Le Dortz, A. Savoy-Navarro  
and P. Schwemling  
*LPNHE, Universités de Paris VI et VII, Paris, France*

L.O. Eek, B. Lund-Jensen and J. Söderqvist  
*Royal Institute of Technology, Stockholm, Sweden*

A. Astbury, R. Keeler, M. Lefebvre, S. Robertson and J. White  
*University of Victoria, British Columbia, Canada*

### **Abstract**

This paper describes the construction of an integrated preshower within the RD3 liquid argon accordion calorimeter. It has a stereo view which enables the measurement of two transverse coordinates. The prototype was tested at CERN with electrons, photons and muons to validate its capability to work at LHC ( Energy resolution, impact point resolution, angular resolution,  $\pi^0/\gamma$  rejection ).

Submitted to *Nucl. Instr. and Meth.*

# 1 Introduction

The RD3 collaboration is pursuing a project towards the construction of a liquid argon electromagnetic calorimeter with accordion geometry for the ATLAS detector at LHC [1]. In previous papers [2], it has been shown that such a calorimeter ('2m prototype') can achieve a good energy resolution with small local constant term,

$$\frac{\sigma_E}{E}(\%) = \frac{(9.99 \pm 0.29)}{\sqrt{E(\text{GeV})}} \oplus (0.35 \pm 0.04) \oplus \frac{(282.2 \pm 16.9)}{E(\text{MeV})}$$

good uniformity ( $.69 \pm 0.05$  % over  $1 \text{ m}^2$ ), and good impact point resolution

$$\sigma_{\eta}(\text{mm}) = \frac{(4.70 \pm 0.05)}{\sqrt{E(\text{GeV})}} \oplus (0.210 \pm 0.015)$$

with cells of size  $\Delta\eta \times \Delta\phi = 0.01764 \times 0.01964$ .

The decay  $H^o \rightarrow \gamma\gamma$  ( $m_{H^o} \simeq 100 \text{ GeV}$ ) gives the toughest constraint on the electromagnetic calorimeter, especially on the direction measurement. Due to the spread of vertices along the beam direction ( $\sigma_z \simeq 5.5 \text{ cm}$ ) and to the mean number of events per crossing (23 at a luminosity of  $10^{34} \text{ cm}^{-2} \text{ s}^{-1}$ ), the  $z$  vertex coordinate of Higgs events has to be reconstructed with the calorimeter. In the azimuthal plane ( $\phi$ ), the small width of the proton beams ( $\leq 30 \mu\text{m}$ ) gives an additional point to the calorimeter one. To achieve an angular measurement which does not degrade the Higgs mass resolution, two points in  $\eta$  and one in  $\phi$  at least, have to be measured by the calorimeter.

In order to preserve the calorimeter performance in the context of a complete detector (including inner tracking and solenoid in front) and to have good  $\gamma/\pi^o$  rejection, the RD3 collaboration has tested with success a highly granular preshower [3][4]; this preshower is called "separate" because it is physically another piece of detector mounted in front of the calorimeter inside the cryostat. The first layer of sensitive liquid argon is after  $2 X_o$  and has cells of size  $\Delta\eta \times \Delta\phi = 0.08 \times 0.0025$ . The second one is after  $3 X_o$  and has cells of  $\Delta\eta \times \Delta\phi = 0.0025 \times 0.08$ . Each layer measures an impact point of electrons in  $\eta$  or  $\phi$  with a precision of 0.3 to 0.4 mm at 50 GeV. Combining the informations from the two layers,  $\pi^o$  with  $p_T=50 \text{ GeV}$  are rejected by a factor greater than 3 (photon efficiency of 90 %) with little dependence on the configuration of disintegration in the  $(\eta, \phi)$  plane. Adding the measurement of the front sampling of the calorimeter behind the preshower, a good angular resolution of 3.5 mrad at 50 GeV is obtained.

The GEM collaboration [8] decided to integrate the preshower within the calorimeter and privileged the  $\eta$  direction since only one more point in  $\eta$  is needed to reconstruct the invariant mass of the decay  $H^o \rightarrow \gamma\gamma$ . It has a depth of a few  $X_o$  in order to measure precisely the position of the shower and its lateral extension, leaving most of the energy in the second compartment to measure a second point with the same accuracy as in the '2m prototype'. Small strips (4.7 mm wide in  $\eta$ ) are made on the electrodes and 24 strips in  $\phi$  are connected together so that the number of cells in the front sampling ( $\Delta\eta \times \Delta\phi = 0.004 \times 0.156$ ) is equal to the number of the middle one ( $\Delta\eta \times \Delta\phi = 0.026 \times 0.026$ ). In such a system, the first sampling acts like an "integrated" preshower aligned naturally with the other part of calorimeter, an important fact for the direction measurement. The low granularity in  $\phi$  is compensated by the high one in  $\eta$  to keep acceptable the  $\pi^o/\gamma$  rejection factor. Such a prototype filled with liquid krypton was tested and gave a resolution in the  $\eta$  direction of 4.5 mrad at 50 GeV for electrons [7].

As with a separate preshower, it is interesting to measure precisely both directions while keeping the advantages of an integrated device. First, most  $\pi^o$  in any configuration in the  $(\eta, \phi)$  plane can be rejected. Second, within the ATLAS detector [9], the solenoid in front of the calorimeter separates photons from electron bremsstrahlung in the  $\phi$  direction. These photons can be disentangled if the calorimeter has a good granularity in the  $\phi$  direction. These facts led us to design and build a "UV" preshower which measures two stereo views of electromagnetic showers.

## 2 Calorimeter setup

### 2.1 Principles of the stereo integrated preshower

As shown with the GEM prototype, the granularity of the calorimeter can be increased in  $\eta$ . But, because of the accordion geometry in  $\phi$ , the minimal size of the cells in  $\phi$  is limited by the amplitude of the accordion waves. For the RD3 prototype, it covers three layers of two liquid argon gaps which leads to  $\Delta\phi = 3 \times 2\pi/960$ . This constraint was bypassed by making cells measuring a linear combination of  $\eta$  and  $\phi$ .

The  $u$  and  $v$  coordinates are defined as related to  $\eta$  and  $\phi$  by the following equations :

$$u = (\eta - \rho\phi)/\sqrt{1 + \rho^2} \quad v = (\eta + \rho\phi)/\sqrt{1 + \rho^2}$$

where  $\rho$  is a free parameter. The combination of the independent measurements of  $u$  and  $v$  (Fig. 1) yields  $\eta$  and  $\phi$  with errors

$$\sigma_\eta^2 = (\sigma_u^2 + \sigma_v^2) \cdot \frac{1 + \rho^2}{4} \quad \sigma_\phi^2 = (\sigma_u^2 + \sigma_v^2) \cdot \frac{1 + \rho^2}{4\rho^2}$$

which implies that  $\rho$  should be close to 1 in order to have comparable precision in both direction.

In order to measure  $u$  and  $v$ , strips with special arrangement are drawn on the first compartment of the electrodes (Fig. 2). Since the border moves in  $\phi$  with depth in the calorimeter because of the accordion shape, it changes in  $\eta$  too.

Each coordinate is measured by its corresponding type of electrodes:  $U$  or  $V$  electrodes have strips with borders constant in  $u$  or  $v$  to measure the  $u$  or  $v$  coordinate. The  $U$  and  $V$  electrodes are interleaved in the transverse plane ( $\phi$ ) in order to share the information given by the electromagnetic shower.

Since the strips on the electrodes are much smaller ( $M$  times) than the cells of the '2m prototype', several  $U$  or  $V$  strips are connected together to keep a reasonable number of channels. Successive  $U$  or  $V$  electrodes are separated in  $\phi$  by an angle of  $2 \times 2\pi/960$ . To connect a strip to the corresponding one on the next electrode of the same type, the following constraint [5] appears :

$$\rho = n \frac{\Delta\eta}{M} \frac{N_{tot}}{4\pi}$$

with  $\Delta\eta$  being the size of the cells in  $\eta$  of the '2m prototype' ( $\Delta\eta = 0.01764$ ),  $N_{tot}$  the total number of electrodes extrapolated to a full circle ( $N_{tot}=960$ ) and  $n$  the distance, in strip unit, between the connected ones on the electrode (Fig. 3). In the context of RD3, to have a good  $\pi^0/\gamma$  separation ( $M=4$ ) and to make  $\rho$  close to 1, we chose  $n=3$  and obtained  $\rho = 1.0107$ . The following sections will show the modifications of the UV electrodes compared to the electrodes of the '2m prototype' [2].

### 2.2 Electrodes with small strips

To have a good  $\pi^0/\gamma$  rejection at 50 GeV, the front sampling was chosen to be four times more granular than the middle one. This leads to a typical strip width as narrow as 5 mm for the strips. It is thus important to minimize the dead space between strips (no electric field). The space between high voltage strips is reduced to 0.5 mm (Fig. 4). But in order to have some tolerance when the two copper-plated kaptons are glued together, the space between signal strips is extended to 1 mm.

The transverse granularity of the middle ( $\Delta\eta \times \Delta\phi = 0.0176 \times 0.0196$ ) and back ( $\Delta\eta \times \Delta\phi = 0.0352 \times 0.0196$ ) samplings were not changed.

The depth of the first sampling is a compromise between the following requirements [6] :

- most of the energy should be contained in one sampling to minimize the contribution of the intercalibration between cells

- the recovery of the energy lost in front of the calorimeter is powerful if the electromagnetic shower is measured in the front sampling with the minimal development in it
- the  $\pi^0/\gamma$  rejection increases with the depth until  $6 X_o$

These requirements have led us to choose a front sampling of  $4.6 X_o$ , a second one of  $12.8 X_o$  and the third one of  $8 X_o$  at  $\eta=0$ . For simplicity sakes, the frontiers between samplings are at constant radius.

### 2.3 High voltage supply to the front sampling

One of the main differences with the electrodes of the '2m prototype' is the high density of signal outputs on the front face of the calorimeter (4 times more). The lack of space forbids to bring directly high voltage to the front face. This problem is solved by bringing high voltage through resistive bridges from the middle sampling to the front one [8]. They are made of resistive ink deposited onto the copper high voltage layer. They are resistive to avoid cross talk between different samplings.

In the LHC environment, the continuous flow of electrons which are evacuated from the high voltage layer to the high voltage supply through these resistors could decrease the voltage of the outer copper layer. To avoid the induced decrease of the drift velocity of electrons and the charge collection, these resistors should not have too high values ( $\leq 10 \text{ M}\Omega$ ). The aim was to get resistances of  $100 \text{ k}\Omega$  but we reached only  $10 \text{ k}\Omega$ . This fact increased the crosstalk between front and middle samplings.

### 2.4 Electronic connections

At the back of the electrodes, the design of the output signals of the middle and back samplings is the same as the standard RD3 electrodes (three consecutive cells in  $\phi$  are connected together).

To have only twice more electronic channels in the first sampling than in the middle one, six strips U(V) with the same U(V) border were connected together following the rules presented in section 2.1. Figure 3 displays the connection scheme.

Pins are soldered onto the electrode outputs to extract the signal from each strip. The strips with the same U(V) borders are summed with summing cards. The first and last pins in  $\phi$  are longer to reach the mother board and connect summing card to the motherboard. This layout needs a radial space of less than 3 cm.

The motherboard of the front face is a multilayer card. In the 1994 run, they were equipped with monolithic GaAs pre-amplifiers [10]. In the 1995 run, some of the motherboards were modified for silicon preamplifiers laying outside of the cryostat (0T) [11].

### 2.5 Test beam layout

A sector of the '2m prototype' has been modified to accommodate the new electrodes with the UV geometry. The UV sector covers  $0.42 \leq \eta \leq 0.85$  and a  $\Delta\phi = 0.157 \text{ rad}$ . It contains 188 channels in U, 188 in V, 192 in the middle sampling and 96 in the back one. The active part of the calorimeter begins at a radius of 1348 mm and ends at 1793 mm.

During 1994, this prototype was tested in the H8 beamline of the CERN SPS with electrons of energy between 10 to 200 GeV and with photon energies ranging from 10 to 100 GeV. Muons were also present in the 200 GeV beam of electrons.

The beam line was equipped with two fast scintillation counters used for the trigger, two slow scintillation counters in the beamline well before the calorimeter and three proportional wire chambers from which the impact point of the electron in the calorimeter was extrapolated.

Table 1 gives the depth of each sampling in  $X_o$  at  $\eta=0.67$  which is the studied point. In front of the preshower, there is  $1.2 X_o$  ( $\eta=0$ ) coming mainly from the iron of the wall of the cryostat (8 mm) and from the liquid argon (8.3 cm defined mainly by the space used by the summing cards and the preamplifiers) in front of the active part of the calorimeter.

$\eta$	Inactive matter	Sampling UV	Mid. Sampling	Back Sampling
0.67	1.5	5.9	15.8	9.9

Table 1: Number of  $X_o$  for each sampling

### 3 Electronic noise and muon signal

#### 3.1 Electronic noise

Pedestals and electronic noise are measured with random triggers during each run. The gains are measured with calibration pulses as already done for the '2m prototype'.

Table 2 presents the noise measured for cold (GaAs) and warm (outside the cryostat) preamplifiers for clusters of channels used for the energy analysis (see section 5). The high noise for the middle sampling with cold electronics was due to oscillations of the GaAs preamplifiers. The oscillations were cured for the 1995 testbeam run (12 MeV per cell for samplings U and V, 50 MeV and 52 MeV for the middle and back samplings mostly incoherent).

Electronic	Sampling U	Sampling V	Mid. Sampling	Back Sampling
GaAs	108 MeV	104 MeV	262 MeV	170 MeV
0T	120 MeV	145 MeV	180 MeV	235 MeV

Table 2: Noise contributions of the different samplings and different electronics

Table 3 shows the values of crosstalk measured with calibration pulses between neighboring cells in  $\eta$ . The crosstalk in  $\phi$  was not measured and assumed to be negligible. An electrical simulation shows that the lateral crosstalk between strips is mostly capacitive. The crosstalk between front and middle samplings goes through the resistive ink. All the energies are corrected for the crosstalk effect in the following analysis. These corrections equalize the gains between U and V cells and make the observed shower width smaller (better  $\pi^0/\gamma$  rejection).

	Samp U	Samp V	Middle Samp.	Back Samp.
Samp. U	1.8%	-	1%	0%
Samp. V	-	1.5 %	1%	0%
Samp. Middle	0.5%	0.3%	0.5%	0.5%
Samp. Back	0%	0%	0.5%	-

Table 3: Values of crosstalk from columns to lines

#### 3.2 Muon signal

In this section, we consider the muon signal in the UV sampling only. Muons are selected from the 200 GeV electron data, where the muon contamination is high ( $\simeq 12\%$  of the events). The following selection criteria have been applied: the energy deposited in the front sampling (normalized to the electron energy) is lower than 25 GeV, one impact point per beam chamber is required and the three points fit a straight line with a good  $\chi^2$ . The cluster of energy of the muon is reconstructed as 2 cells in each sampling (U and V): the first cell is the one which is pointed to by the beam extrapolation

in the calorimeter ( $\eta_{beam}$  or  $\phi_{beam}$ ); the second cell is the next closest to the extrapolated beam impact point. The energy deposited by the muon in the front sampling is the sum of the energies reconstructed in the 4 cells (2U+2V). Figure 5 shows the muon energy compared to noise for the run at  $\eta = 0.67$ . The signal to noise ratio is measured to be 2.9 for a peaking time for the triangle of  $\simeq 45$  ns between 5 to 100%.

The  $u$  and  $v$  barycenters of the two cells are combined to compute the  $\eta_{uv}$  and  $\phi_{uv}$  coordinates of the muon. Figure 6 shows the two distributions  $\eta_{uv} - \eta_{beam}$  and  $\phi_{uv} - \phi_{beam}$  for muons; the position resolution in  $\eta$  ( $\phi$ ) is  $\simeq 1.9$  mm (1.7 mm) is very close to the width of the strips (6 mm) divided by  $\sqrt{12}$ . This is expected as most of the muon energy is deposited in one strip.

## 4 Shower profiles

### 4.1 Individual and mean lateral profiles.

Figure 7 shows a typical individual profile of a  $\gamma$  of 100 GeV in the front sampling on U electrodes (see section 8).

In order to get mean profiles of the electromagnetic shower, we have proceeded in the following way. A histogram is made with a binning much smaller (by a factor of 5) than the actual strip width. For each event, the content of each strip, normalized to the total energy, is histogrammed as a function of the difference between the strip number and the barycenter of the shower. This allows us to unfold the beam spot width from the lateral one of the electromagnetic shower. The mean profile (Fig. 8) has been fitted with the function:

$$\frac{c}{1 + \left(\frac{x-x_0}{a}\right)^2}$$

The constant  $a$ , found to be equal to 0.70 in strip unit, is the ratio between the half width of the electromagnetic shower and the strip size. Since the strips in the front sampling have a width of the same order as the gap width between the absorber and the electrode (1.9 mm), the induced current on neighboring strips becomes significant. This spread effect has to be simulated in order that the Geant simulation gives a width ( $a = 0.76 \pm 0.02$ ) compatible with the data. The impact point of the electron on the calorimeter can be measured precisely using the lateral distribution of the shower since its width is of the same order as the width of the strips.

### 4.2 Longitudinal profile

Figure 9 shows the sharing of the shower energy between the samplings for electrons of 200 GeV. There is about one third of the energy deposited in the preshower and most of the remaining in the middle sampling. At 10 GeV, two thirds of the energy are deposited in the front sampling. The barycenters in depth of the shower for the first two samplings were estimated, with simulation, to be at radii of 1.41 and 1.51 m.

The agreement between data and simulation is not totally satisfactory especially for tails in the two samplings. This disagreement will be discussed in the following sections.

## 5 Energy resolution and linearity

The total energy is defined as the sum of the energies of the clusters of each sampling. The U and V clusters are the 11 contiguous cells (same size as the middle sampling) centered on the most energetic one in  $\eta$  (Su11+Sv11). The common zone covered by the U and V clusters has the same size as the nonet of the middle sampling. The cluster of the middle sampling is a nonet of cells centered on the most energetic one ( $S_{mid.}$ ). The cluster at the back is just behind the cluster of the middle sampling and contains  $2 \eta \times 3 \phi$  cells ( $S_{back}$ ).



It exists a strong anticorrelation between the total energy and the energy deposited in the front sampling (U+V) (Fig. 10). When the energy in the preshower is large, it means that the electromagnetic shower started at the beginning of the calorimeter and lost some energy during its travel across 'dead' matter in front.

One can compensate for this loss by multiplying the energy deposited in the UV sampling by a factor  $1+\alpha$ . For the data, the fitted value is  $\alpha=0.14$  for all energies. The total energy of the shower is computed as :

$$E = (1 + \alpha)(Su11 + Sv11) + S_{mid.} + S_{back}$$

The disagreement between simulation ( $\alpha=0.09$ ) and data for the slope could be explained by a inaccurate simulation of the shower development and an underestimation of the matter in front of the active part of the calorimeter (at least  $0.3 X^o$  in the beam line is neglected in the simulation).

## 5.1 Geometrical corrections to energy measurement

The corrections to the  $\eta$  and  $\phi$  modulations which will be applied to the energy measurement are similar to those of a accordion calorimeter without integrated preshower [2].

Figure 11 shows the dependence in  $\phi$  (amplitude  $\pm 1$  %) of the total energy. The shape can be parameterized with sinusoidal functions of periods submultiple of the middle sampling cell size:

- 1 which corresponds to the fact that, at the edge of the central cell, less energy is contained in the nonet than at the middle of the cell
- 1/3 and 1/6 which correspond to the period in the distribution of matter with the accordion geometry
- 2/3 which is the period of U or V electrodes (zone of containment is different)

The first two periods already exist in the '2m prototype' and the last one is specific to the UV geometry. Figure 11 shows the dependence in  $\eta$  (amplitude of  $\pm 0.5$  %): as in the case of  $\phi$ , more energy is contained when the particle hits at the center of the central cell of the nonet in  $\eta$ . A parabolic correction is applied to correct the  $\eta$  dependence.

## 5.2 Energy resolution and linearity

Electrons of good quality were selected by requiring a minimum energy deposited in the four scintillators and only one point seen in each beam chamber. The energy beam spread was unfolded (0.287 % at 200 GeV). For the fit of the energy resolution (Fig. 12), the contribution of the noise term was fixed at the value measured with random triggers.

The fits give the following results with the electronic noise fixed at the values of table 2:

$$\frac{\sigma_E}{E} (\%) = \frac{(11.62 \pm 0.10)\text{GeV}^{1/2}}{\sqrt{E}} \oplus (0.0 \pm 0.15)$$

For the energy resolution, data and simulation are in agreement when the corresponding values of  $\alpha$  are used. The sampling and constant terms are comparable to the one previously published [2].

For the study of the linearity, the corrections determined at 200 GeV were applied at all other energies. Figure 13 shows the ratio of the measured energy to the real energy and the same normalized to the same ratio in the Geant simulation. The ratios have been normalized to 1 for electrons of 200 GeV. The data point are within the mean beam momentum uncertainty ( $\Delta P/P=25\%/P(\text{GeV}) \oplus 0.5\%$ ) except at low energy. The simulation reproduces these non linearities at low energy within the beam energy uncertainty.

## 6 Position and direction resolutions

### 6.1 Evaluation of the resolution

For a given sampling in depth  $S_i$ , the resolution in position is evaluated from the comparison between the predicted impact point according to the beam chambers ( $x_{BC}^{S_i}, y_{BC}^{S_i}$ ) of the incident particle with the measured position of the shower ( $x_{calo}^{S_i}, y_{calo}^{S_i}$ ):

The predicted impact point is extrapolated with the line fitted to the points measured in the three beam chambers ( $\sigma_{x,y} \simeq 100 \mu\text{m}$ ). The extrapolation was calculated at a radius corresponding to the average longitudinal shower position as computed by simulation for each sampling.

If we consider a cluster of  $\pm N$  strips located around the most energetic one, the impact point position is given by the barycenter of the energies measured in the strips. In the case of UV strips, a cluster size of  $\pm 1$  strip around the most energetic one has been considered because it gives a good resolution (Fig. 14) with a small number of channels.

### 6.2 Resolution in position in the UV sampling.

Concerning the UV sampling, the U (V) strips were considered separately with respect to the beam extrapolation. We have corrected the obtained distributions for effects like the clusterization, S-shape effect (Fig. 15) at 200 GeV. The correcting functions are of the form:

$$w_{corr} - w = a_1 + a_2 \times w_{cell} + a_3 \times w_{cell}^2 + a_4 \times w_{cell}^3$$

where  $w$  stands for  $u$  or  $v$  barycenters in cell units,  $w_{cell}$  is the barycenter position in the central  $u$  ( $v$ ) cell. In the Monte Carlo, the correction factors are similar and describe a purely geometrical effect.

After these corrections, there remains a structure in the difference  $\Delta w = w_{beam} - w_{corr}$  (Fig. 16) versus  $\phi_{uv}$  ( $\phi_{uv}$  reconstructed from  $u$  and  $v$  measured in the first sampling).

The additional correction functions are fitted on the data at 200 GeV:

$$\begin{cases} a_1 \times w_{mod} + a_3 & \text{if } w_{mod} < w_0 \\ \beta \times \frac{T - w_{mod}}{T - w_0} + a_3 & \text{if } w_{mod} \geq w_0 \end{cases}$$

where  $T$  is the U (V) electrode period:  $T = \frac{2}{3} \times \Delta\phi = \frac{2}{3} \times 0.0196$  rad;  $w_0$  is the sub-period inside the cell:  $w_0 = \frac{2}{3} \times T$  for  $v$  and  $w_0 = \frac{1}{3} \times T$  for  $u$ ;  $w_{mod}$  is the position of  $w$  expressed in fraction of  $T$  unit.

This modulation in  $\phi$  due to the geometrical arrangement of the calorimeter is reproduced by the simulation. However it has a smaller amplitude probably due to some mechanical effects and/or a bad description of the induced current on the UV electrodes in the corners of the accordion shape.

The correction functions determined at 200 GeV, are used to correct data at all energies. Impact point resolutions of  $\eta$  or  $\phi$  measured with the UV preshower, are obtained from the distributions of figures 17 where are plotted  $d\eta = \eta_{uv} - \eta_{beam}$  and  $d\phi = \phi_{uv} - \phi_{beam}$ . The beam chamber extrapolation resolution ( $300 \mu\text{m}$  at 200 GeV) is subtracted in order to obtain the calorimeter resolution. Figure 18 shows the impact point resolution as a function of the energy.

The fitted function are :

- for  $\eta$

$$\sigma_{\eta}(\text{mm}) = \frac{(1.8 \pm 0.1)}{\sqrt{E(\text{GeV})}} \oplus (0.179 \pm 0.009) \oplus \frac{(7.7 \pm 0.4)}{E(\text{GeV})}$$

- for  $\phi$

$$\sigma_{\phi}(\text{mm}) = \frac{(2.2 \pm 0.1)}{\sqrt{E(\text{GeV})}} \oplus (0.163 \pm 0.01) \oplus \frac{(4.8 \pm 0.6)}{E(\text{GeV})}$$

The term proportional to  $1/E$  is due to the fact that the fraction of energy deposited in the UV sampling is not constant with the momentum of the electron, due also to multiple scattering in the cryostat and, to a lesser extent, to electronic noise.

The simulation predicts a resolution in  $\eta$  and  $\phi$  better than  $200 \mu\text{m}$  compared to  $250 \mu\text{m}$  in the data at  $200 \text{ GeV}$ . The positioning of the electrodes ( $250 \mu\text{m}$  precision) might explain the small degradation.

At low energy, the position resolution is worse in the data than in the simulation. It might come from a bad description of the shower in the simulation (multiple scattering) as already mentioned in section 5.

### 6.3 Resolution in position in the middle sampling.

The resolution in  $\eta$  and  $\phi$  has also been evaluated for the middle sampling. The barycenter of the nonet centered on the most energetic cell is used. The distributions have been corrected for the S-shape in  $\eta$  and for the observed structure in  $\phi$  (see Fig. 19). The S-shape has been corrected with the function:

$$\eta_{corr} - \eta_{cell} = \delta\eta - p_1 + \frac{0.5 \times \Delta\eta_{cell}}{\tan^{-1}(0.5 \times \Delta\eta_{cell}/p_2)} \cdot \tan^{-1}((\delta\eta + p_3 \cdot \delta\eta^2)/p_2)$$

where  $\eta_{cell}$  being the barycenter in  $\eta$  in the middle sampling,  $\eta_{mid}$  being the middle of the cell in radian,  $\Delta\eta_{cell}$  is the width of the cell in rapidity unit ( $0.01764$ ) and  $\delta\eta = \eta_{cell} - \eta_{mid}$  i.e. the position inside the cell. The coefficients  $p_i$  are fitted to the data at  $200 \text{ GeV}$ .

The  $\phi$  correction is of the form :

$$\phi_{corr} - \phi_{cell} = p'_1 + p'_2 \cdot \delta\phi + p'_3 \cdot \delta\phi^2$$

with  $\delta\phi$  the position inside the cell. This correction is not symmetric around the center of the cell because of the accordion geometry : it is a convolution of the development of the electromagnetic shower with the border of the cell which depends on the depth of the calorimeter. Figure 20 presents the results :

- for  $\eta$

$$\sigma_{\eta}(\text{mm}) = \frac{(5.8 \pm 0.1)}{\sqrt{E(\text{GeV})}} \oplus (0.0 \pm 0.02) \oplus \frac{(30. \pm 0.5)}{E(\text{GeV})}$$

- for  $\phi$

$$\sigma_{\phi}(\text{mm}) = \frac{(5.5 \pm 0.1)}{\sqrt{E(\text{GeV})}} \oplus (0.218 \pm 0.02) \oplus \frac{(24. \pm 0.5)}{E(\text{GeV})}$$

The  $1/E$  term has the same origin as for the UV resolution. The position resolution in the middle sampling is better than  $1 \text{ mm}$ , for electrons with  $E_T=50 \text{ GeV}$ , both in  $\eta$  and  $\phi$ . This can be compared to the  $0.4 \text{ mm}$  obtained for the front sampling. The resolution of the middle sampling is comparable to the one of the first sampling of the '2m prototype'[2].

## 7 Angular resolution

The angular resolution is obtained by comparing the beam direction with the one measured by the calorimeter when combining the information coming from the UV preshower and the middle sampling. The effect of the beam divergence ( $<3 \text{ mm}/10 \text{ m} = 0.3 \text{ mrad}$ ) is negligible compared to the angular resolution of the calorimeter ( $\simeq 0.5 \text{ mm}/10 \text{ cm} = 5 \text{ mrad}$ ). The level arm is  $\Delta R = R_{middle} - R_{uv} = 0.1 \text{ m}$  ( $R_{uv}=1.41 \text{ m}$  and  $R_{middle}=1.51 \text{ m}$ ).

Figure 21 presents the angular resolution :

- for  $\eta$

$$\sigma_{\eta}(\text{mrad}) = \frac{46 \pm 2}{\sqrt{E(\text{GeV})}} \oplus (1.5 \pm 0.4) \oplus \frac{(240 \pm 6)}{E(\text{GeV})}$$

- for  $\phi$

$$\sigma_{\phi}(\text{mrad}) = \frac{48 \pm 2}{\sqrt{E(\text{GeV})}} \oplus (1.8 \pm 0.4) \oplus \frac{(182 \pm 8)}{E(\text{GeV})}$$

The angular resolution is dominated by the resolution of the middle sampling (1 mm at 50 GeV compared to 275  $\mu\text{m}$  for the front sampling). Since the back sampling lays after 23.2  $X_0$ , it does not contain enough energy to improve the middle resolution by combining its measurement to the other samplings.

In conclusion, the precision on the electromagnetic shower direction, determined with the calorimeter information only, is equal to 8 mrad at 50 GeV and is better than 6 mrad above 100 GeV.

## 8 $\pi^0/\gamma$ separation

In this section, we estimate the  $\pi^0/\gamma$  rejection using photons from test beam data. The  $\pi^0$  sample is a combination of two photon events with the right kinematic properties and a total  $p_T$  of 50 GeV (or  $E_{\pi^0} = 60$  GeV at  $\eta=0.67$ ).

Figure 22 shows the test beam setup to obtain photons. A 0.1  $X_0$  layer of aluminum is used as a radiator. The electrons are then deviated by a magnetic field to separate them from the photons. Events with several photons are more frequently converted in a 1  $X_0$  layer of lead than events with one photon (the converted photons are vetoed by the scintillator S2). This property enables us to enrich the sample of 'single' photon events. According to the simulation, a purity of 80% of single photon events is obtained in an energy range from 5 to 60 GeV.

Neutral pions are then constructed by choosing randomly a pair of photons satisfying :

- $E_{\gamma_1} + E_{\gamma_2} = 60 \pm 4$  GeV
- $d_{\gamma_1\gamma_2} = R_{uv} \cdot \frac{m_{\pi^0}}{\sqrt{E_{\gamma_1} \cdot E_{\gamma_2}}} \pm 250$   $\mu\text{m}$

where  $E_{\gamma_1}$  and  $E_{\gamma_2}$  are the energies of the photons and  $d_{\gamma_1\gamma_2}$  is the distance between the two photons extrapolated at  $R_{uv}$ . The window in  $d_{\gamma_1\gamma_2}$  is tight because  $d_{\gamma_1\gamma_2}$  is the key parameter for the separation between two clusters.

These  $\pi^0$  events are weighted to get uniform distributions of  $\Delta E = E_{\gamma_1} - E_{\gamma_2}$  and  $\Delta R = \sqrt{\Delta\eta^2 + \Delta\phi^2}$ . Weights are close to one except when  $|\Delta E| > 50$  GeV (low statistics due to low efficiency of the setup for low energy photons).

Since the shower made by two photons separated by  $\simeq 6$  mm, is larger than the one of a single photon, the used criterium  $R_{17}^2$  is the ratio of the energy contained in the two most energetic contiguous U and V cells compared to the sum of the 17 U and 17 V cells centered on the most energetic ones (Fig. 23). It is not more powerful to compare separately U and V ratio. Figure 24 gives :

- rejection factors using events over all the  $|\Delta E|$  range (optimistic method)
- rejection factors under assumption that it is not possible to reject  $\pi^0$  with  $|\Delta E| > 50$  GeV (conservative method)

The rejection power is underestimated due to the increase of the electronic noise by a factor  $\sqrt{2}$  since two uncorrelated events are superimposed. This effect can modify the result only for low energy photons which have already been said to be problematic for the rejection factor.

In conclusion, the rejection factor  $\pi^0/\gamma$  with  $p_T=50$  GeV, is better than 4 for an efficiency of 90 %.

## 9 Conclusion

The results from testbeam data have shown that it is possible to integrate a stereo preshower without degrading the performance of the '2m prototype'(RD3). The energy resolution has the same sampling factor and a similar constant term. The impact point of an electron with an energy of 50 GeV is measured to 0.4 mm in the front sampling and 1 mm in the middle sampling. The angular resolution for an electron of 50 GeV is 9 mrad. The  $\pi^0/\gamma$  rejection factor at  $p_T=50$  GeV was measured to be better than 4 for an efficiency of 90 %.

## References

- [1] B. Aubert et al. (RD3 Collaboration), Nucl. Instr. and Meth. A 309 (1992) 438; A 321 (1992) 467; A 325 (1993) 118.
- [2] D.M. Gingrich et al. (RD3 Collaboration), Nucl. Instr. and Meth. A 364(1995) 290.
- [3] B. Aubert et al. (RD3 Collaboration), Nucl. Instr. and Meth. A 330 (1993) 405.
- [4] R.A. Davis et al. (RD3 Collaboration) Nucl. Instr. and Meth. A 385 (1997) 47.
- [5] J. Colas, S. Jézéquel, B. Mansoulié, *Principles of a stereo preshower integrated in the accordion calorimeter*, ATLAS Internal Note CAL-NO-040, May 4, 1994.
- [6] A. Cravero and F. Gianotti Atlas Internal Note CAL-NO-31
- [7] GEM Technical Design Report, TN-93-262.
- [8] Performance of an accordion Electromagnetic calorimeter with Liquid Krypton Proceedings of the 5th International Conference on Calorimetry in High Energy Physics p 140-148
- [9] ATLAS Technical Proposal CERN/LHCC/94-43
- [10] D.V. Camin, G. Pessina and E. Previtali IEEE Trans. on Nucl. Sci, 40 (1993) pp 759-763
- [11] R.L. Chase, C. de La Taille, S. Rescia, N. Seguin Nucl. Instr. and Meth. A330 (1993) 228-242

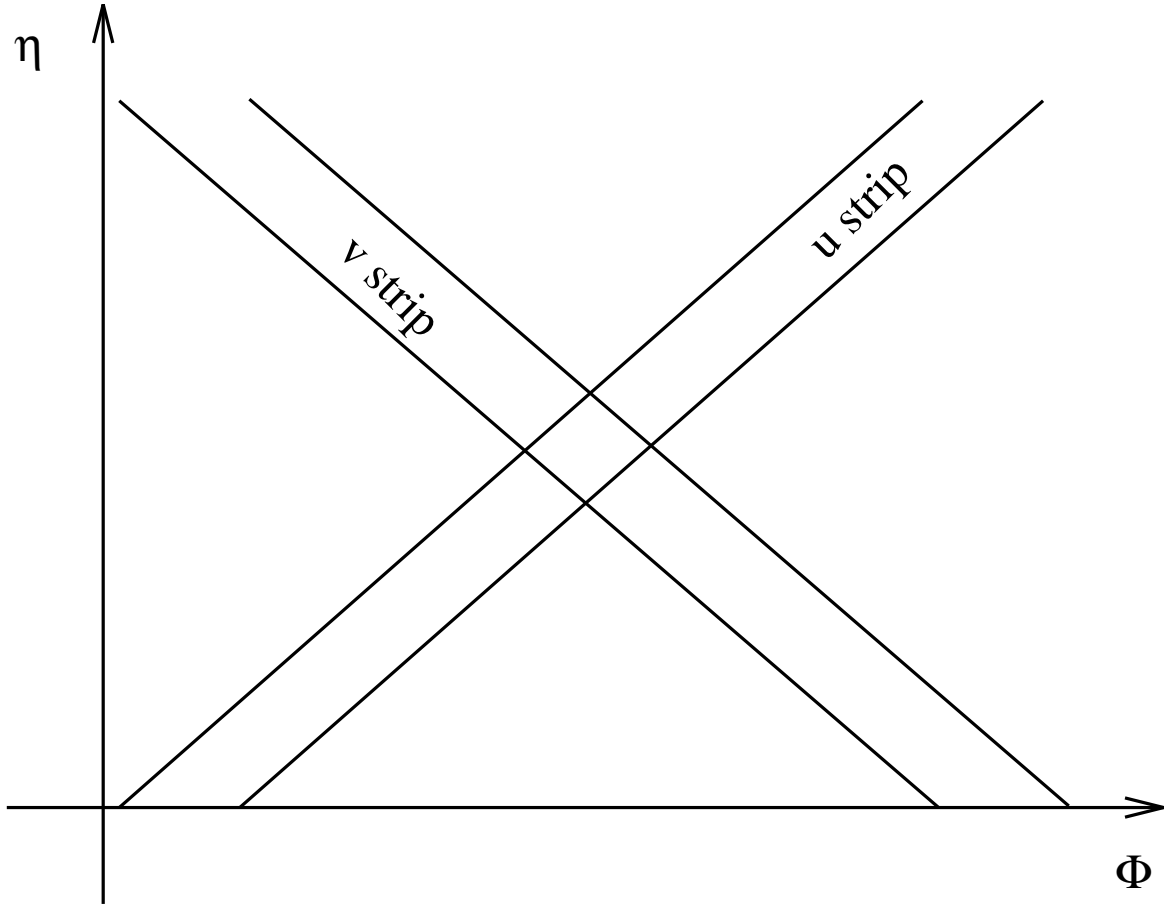


Figure 1: The relationship between U/V strips and  $\eta/\phi$  coordinates for  $\rho \simeq 1$ .

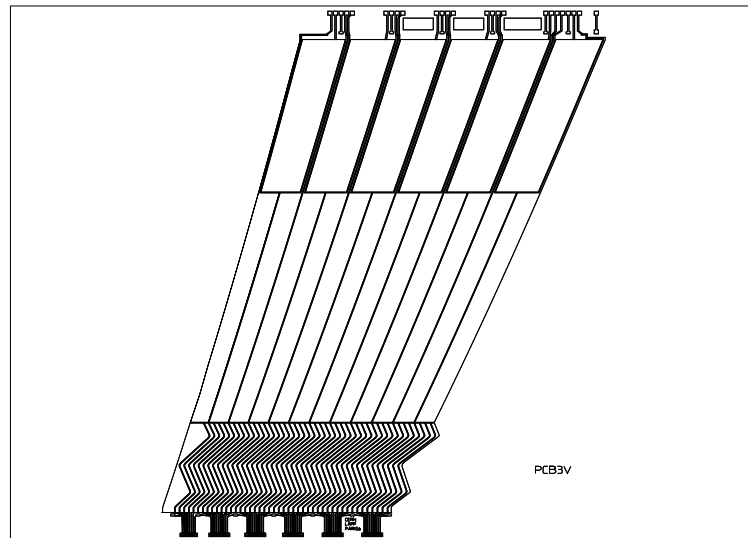
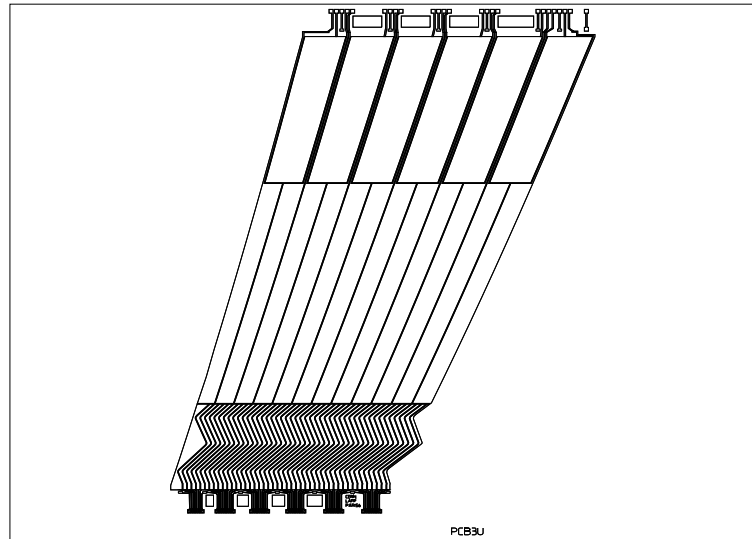


Figure 2: U and V strips disposition on the electrodes, laid flat before the bending in an accordion shape(design from  $\eta=0.42$  to  $\eta=0.63$ ).

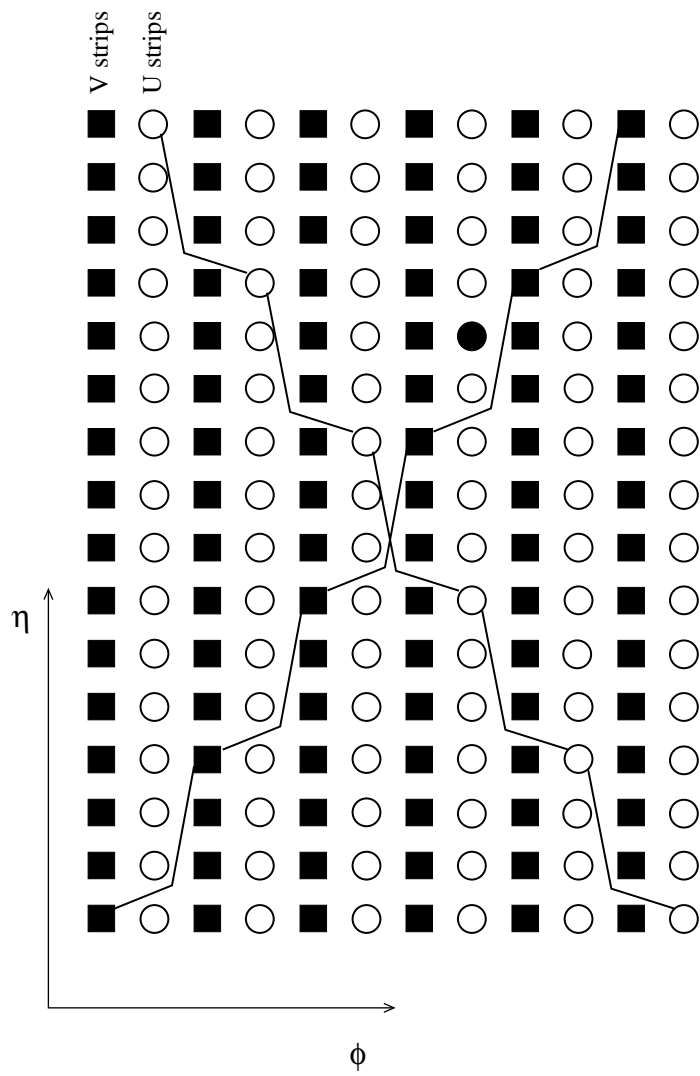


Figure 3: Connection scheme ( $n=3$ )



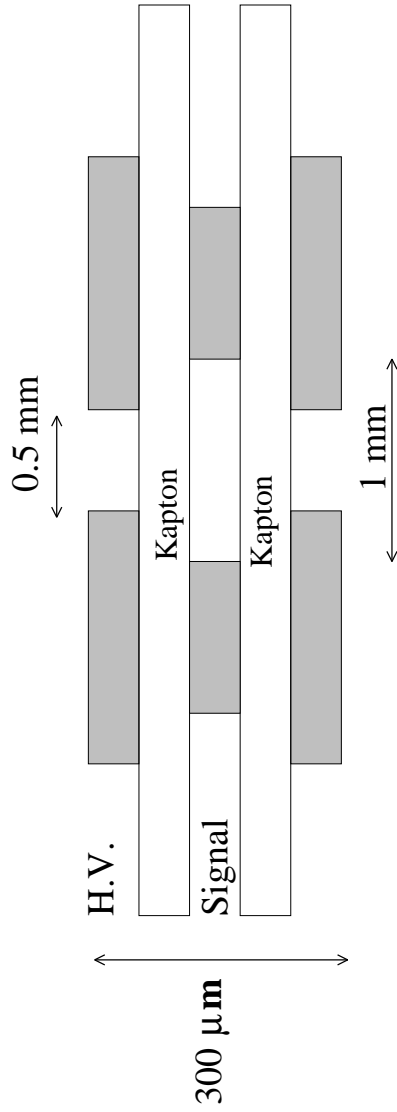


Figure 4: Transverse cut of an electrode (the grey areas are the copper pads).

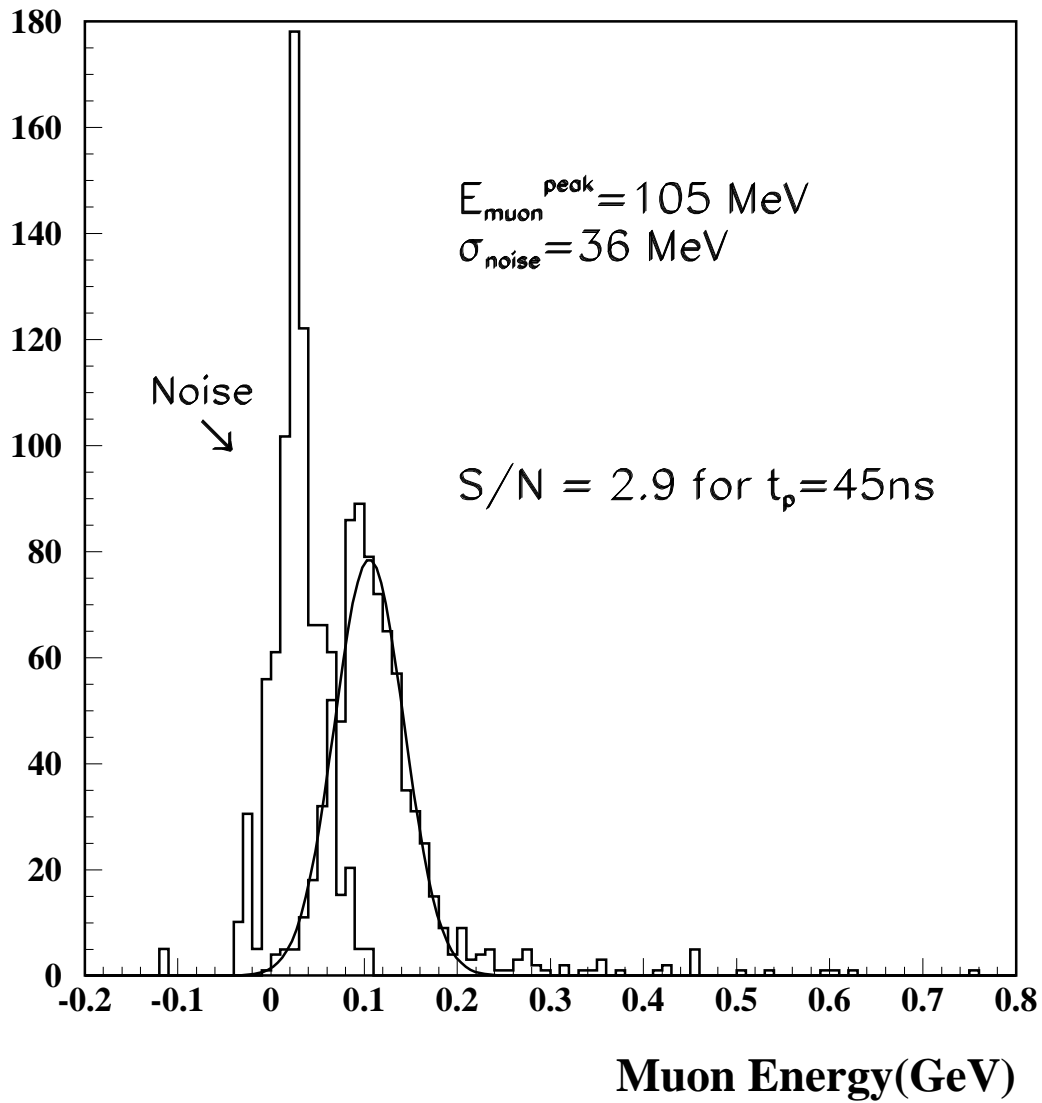


Figure 5: Muon energy reconstructed in the UV sampling ( $E_\mu=200 \text{ GeV}$ )

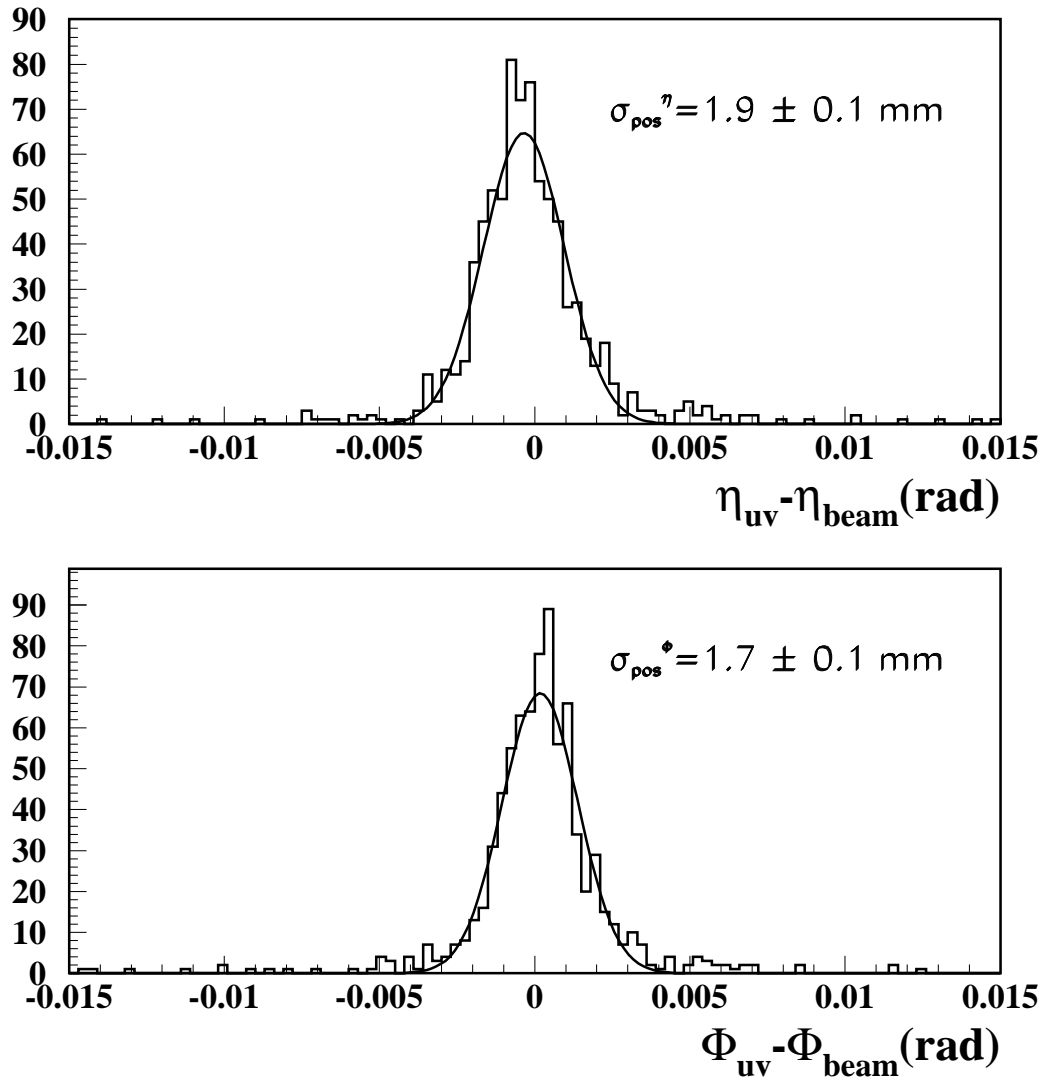


Figure 6: Resolution in position for muons in the UV sampling.

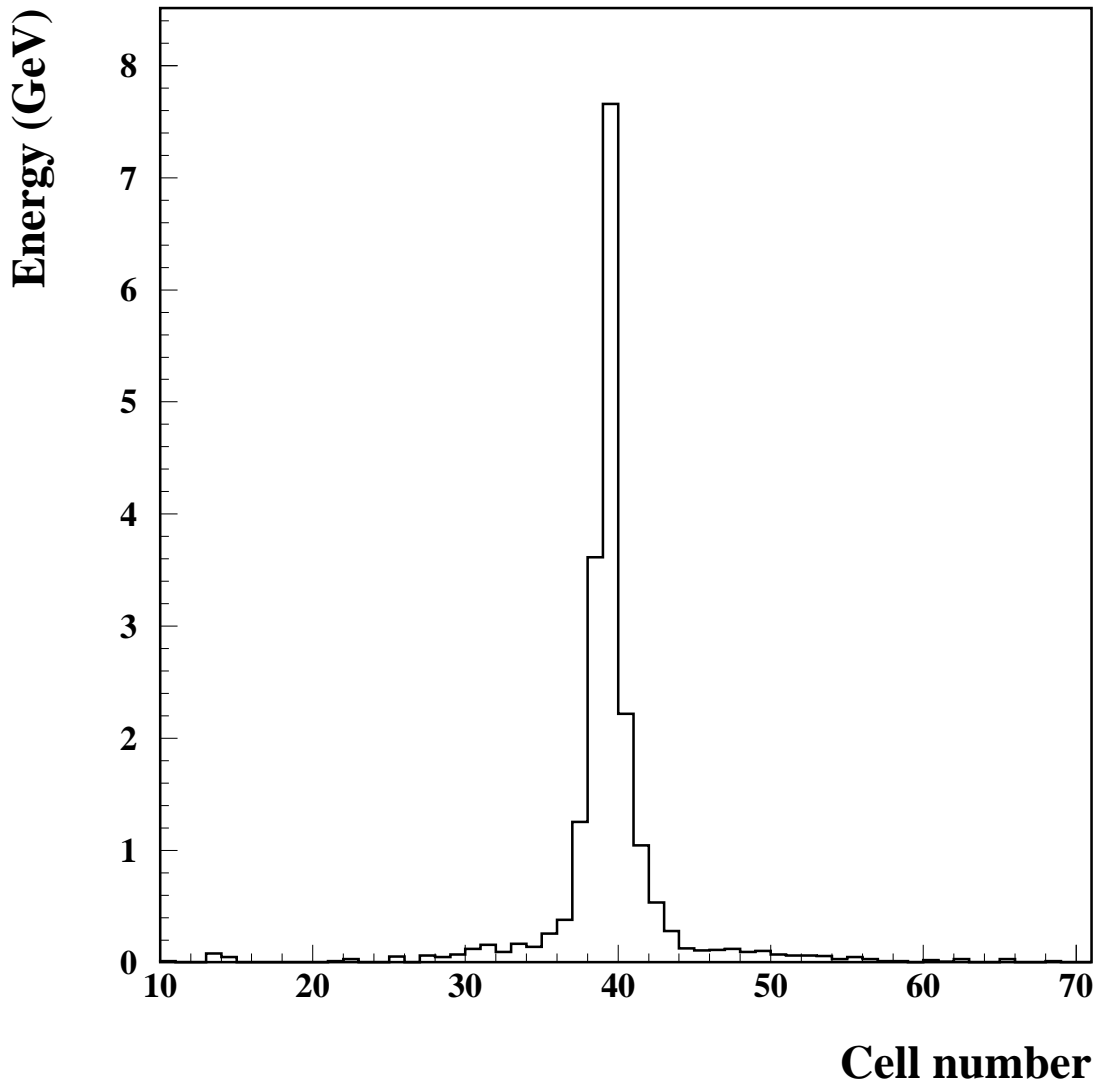


Figure 7: Individual profile in the U direction of a  $\gamma$  (100 GeV).

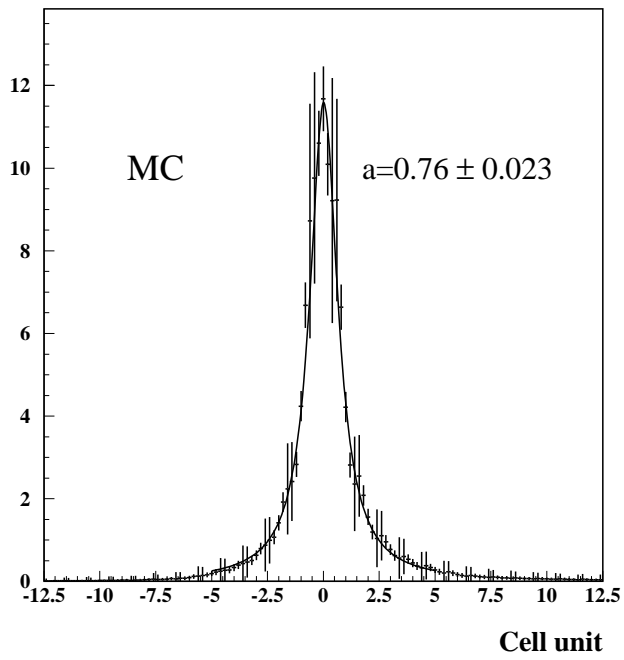
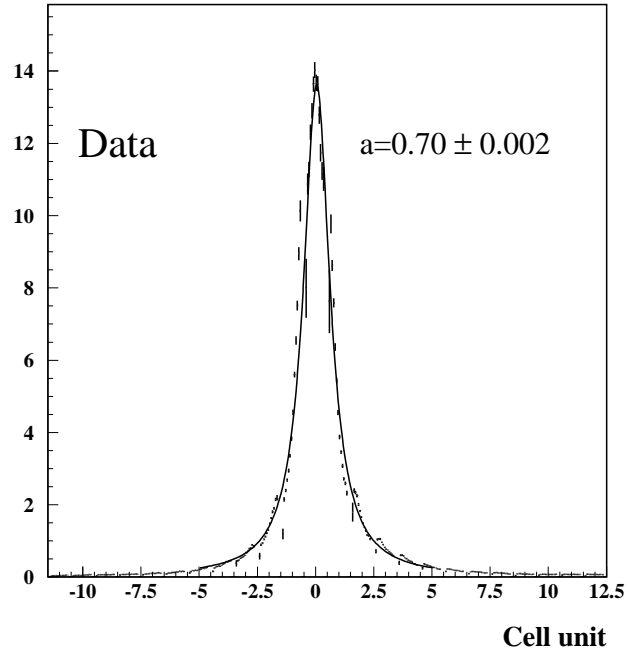
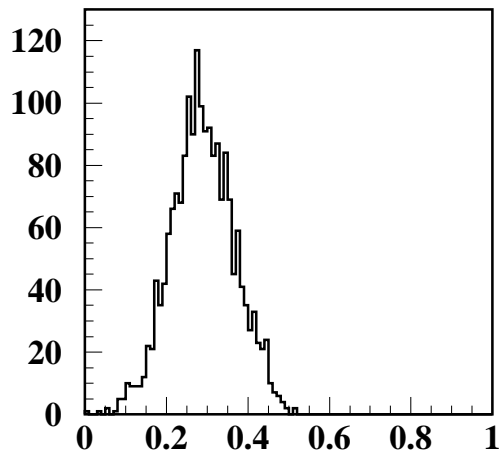
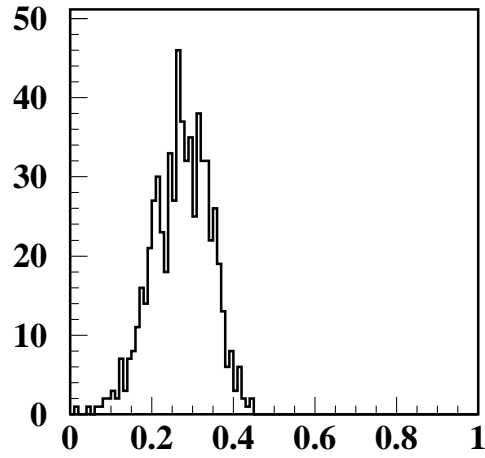


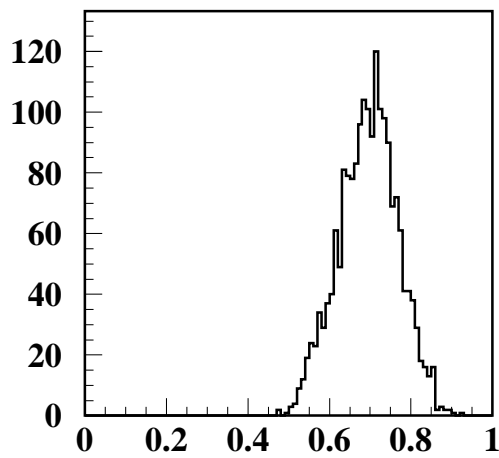
Figure 8: Mean profiles in the U direction of an  $e^-$  at 200 GeV (Data and Monte-Carlo).



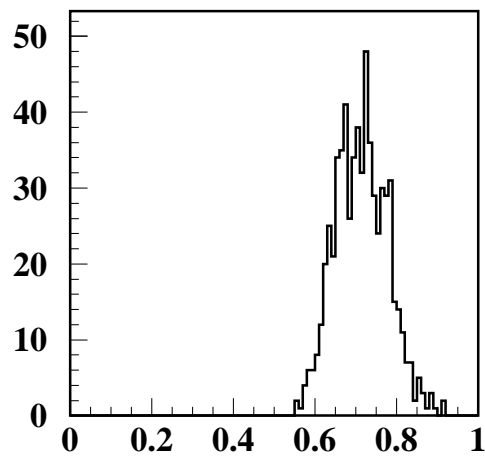
**Front Sampling (Data)**



**Front Sampling (MC)**



**Middle Sampling (Data)**



**Middle Sampling (MC)**

Figure 9: Distribution of the fraction of energy of electromagnetic clusters in the front and middle sampling for Monte Carlo and Data (200 GeV electrons).

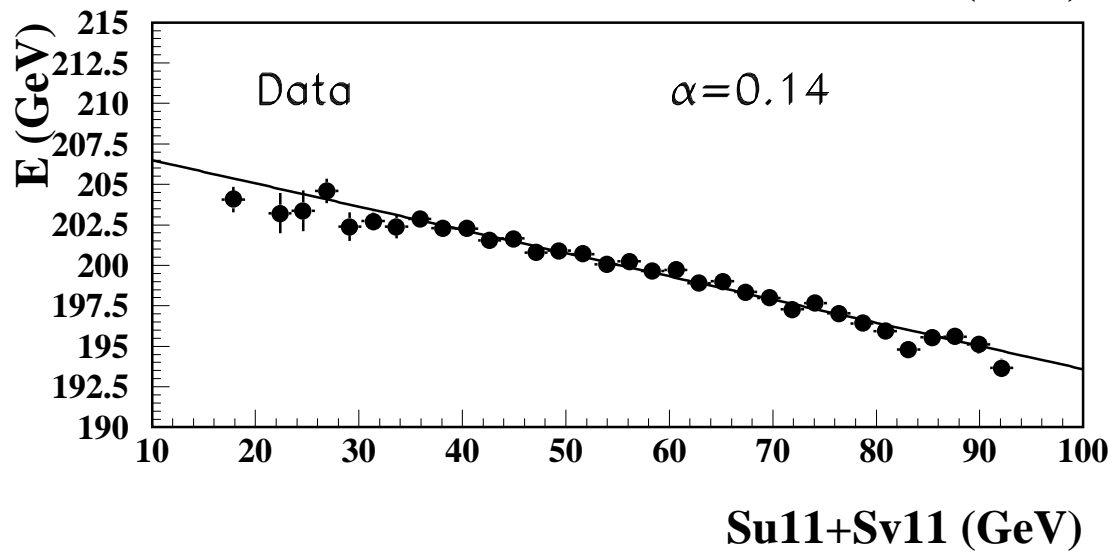
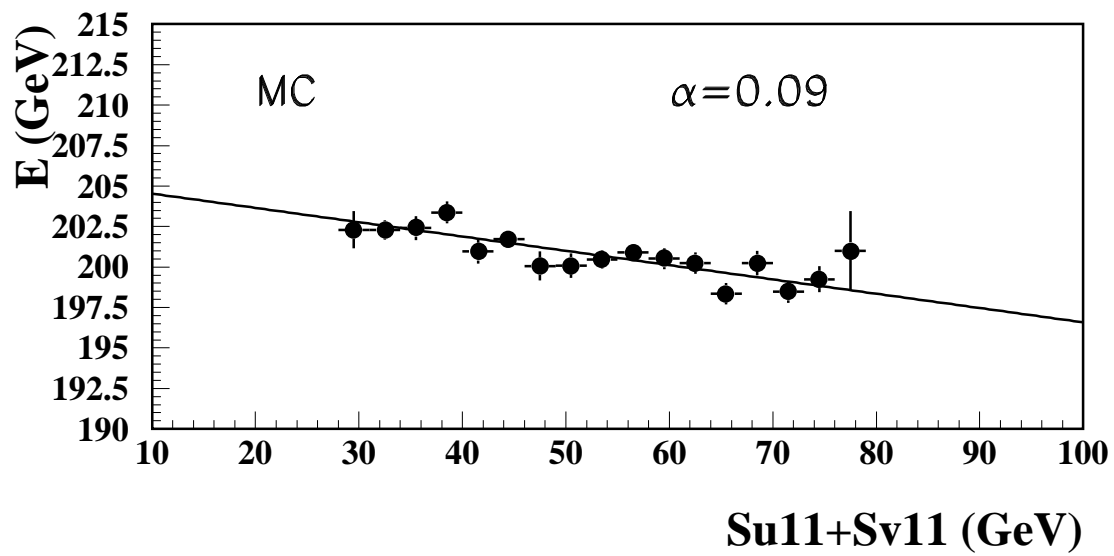


Figure 10: Correlation between energy in the UV sampling and total energy for data and Monte-Carlo for electrons of 200 GeV

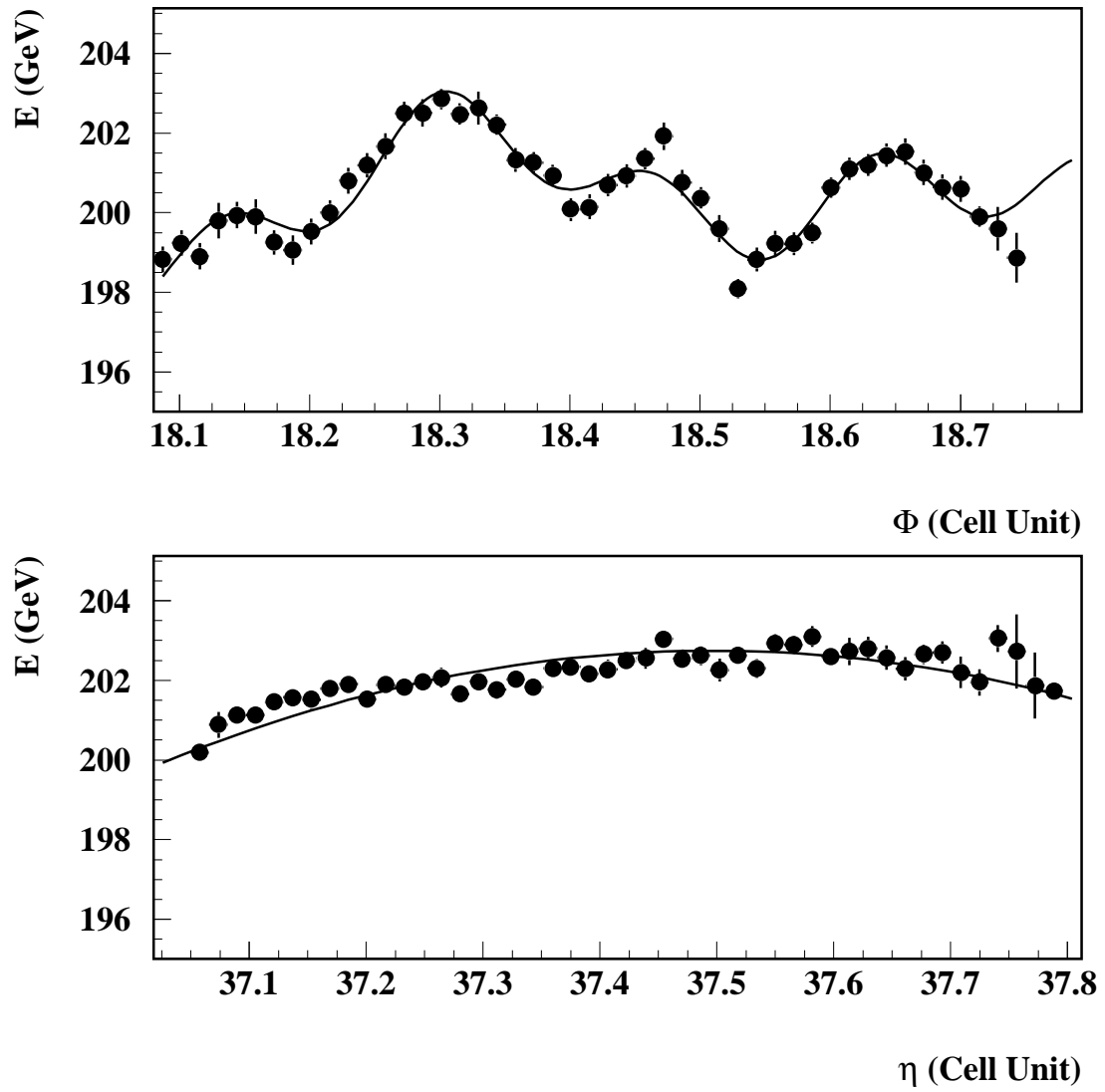


Figure 11: Modulation in  $\phi$  and in  $\eta$  of the energy deposited in the calorimeter.



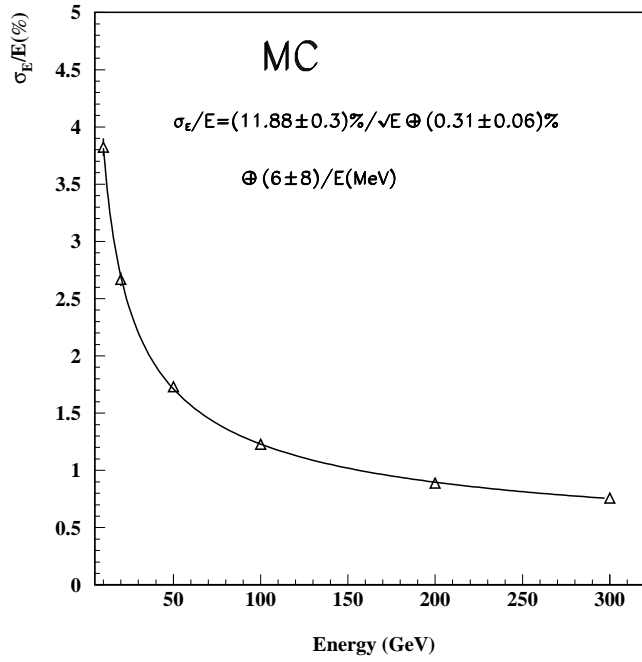
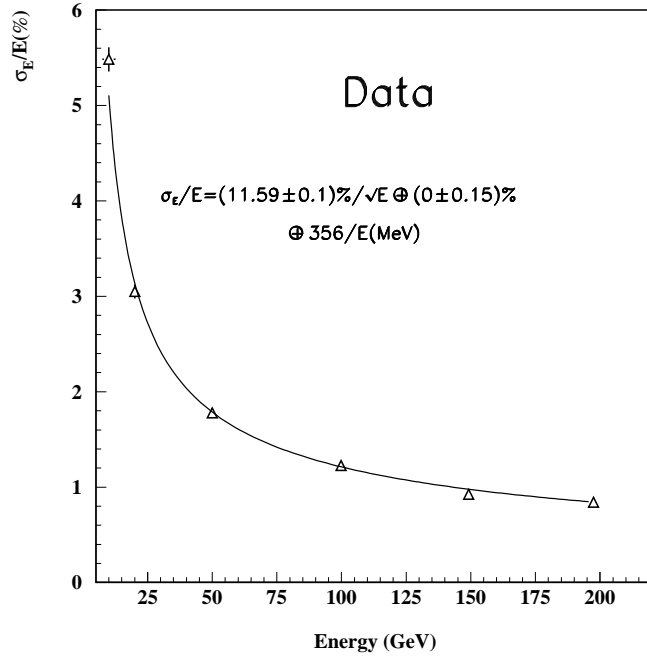


Figure 12: Energy resolution as a function of energy (GaAs). For the data, the noise contribution was fixed to the measured values with random triggers (356 MeV); for the simulation, it was fitted and found compatible with zero as expected.

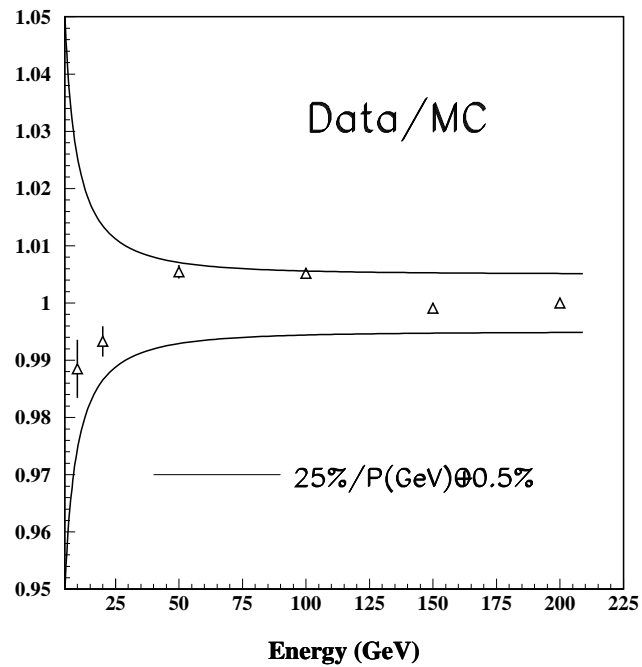
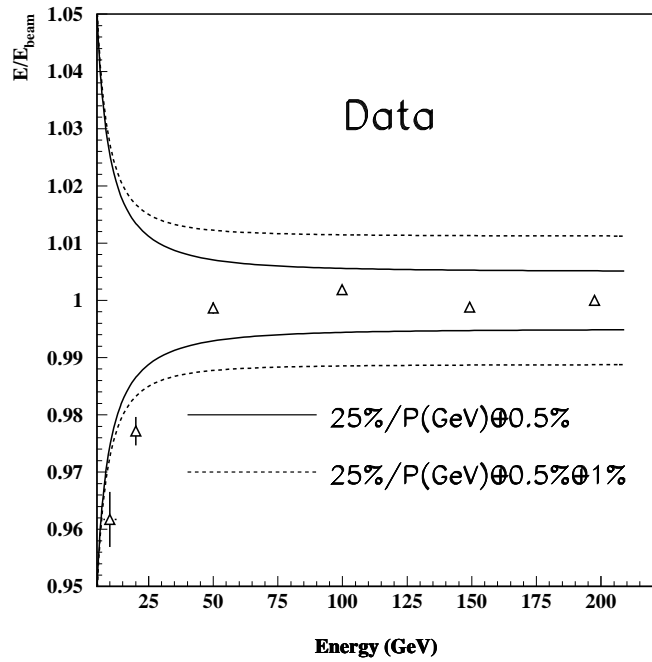


Figure 13: Linearity as a function of energy for data and data/simulation. The full lines define the beam uncertainty area. A 1% non linearity is added quadratically to the beam uncertainty (dashed lines).

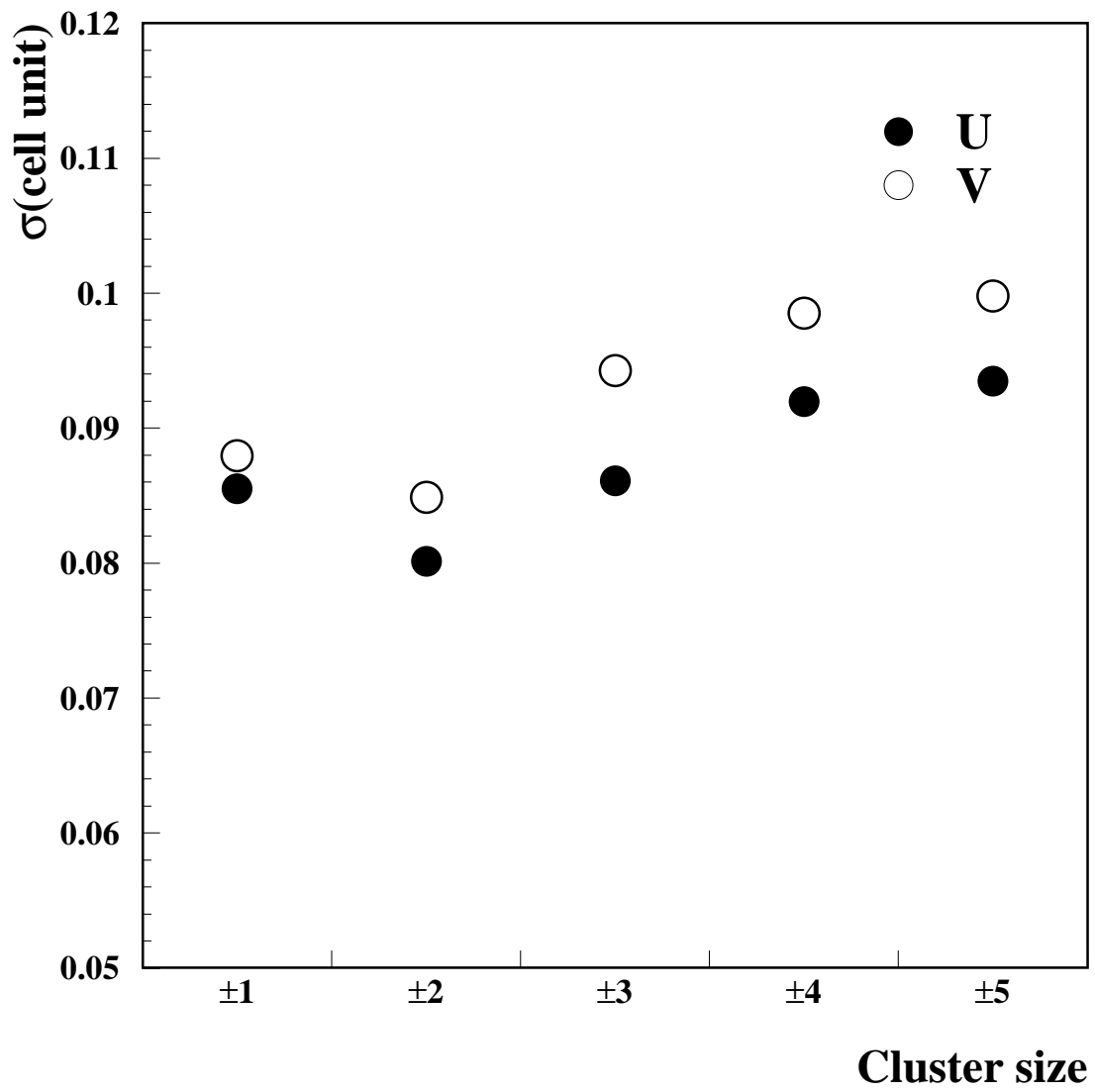


Figure 14: Position resolution as a function of cluster size ( $E=200$  GeV)

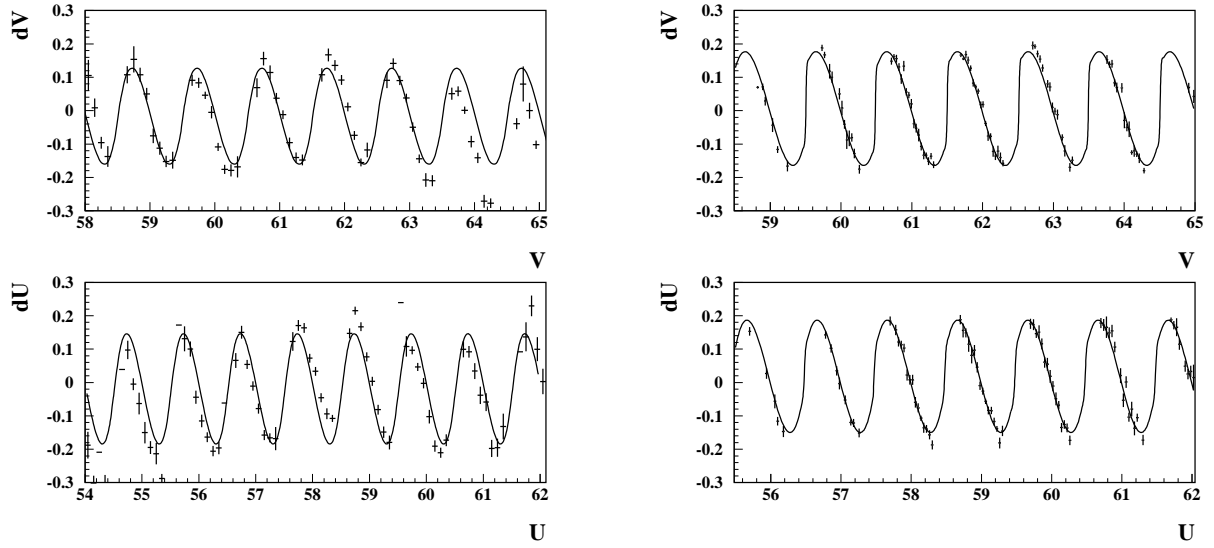


Figure 15:  $w - w_{beam}$  vs  $w$  ( $w=u$  or  $v$ ) before any correction (crosses), and correction function (full line). Numbers are in  $U$  and  $V$  cell units. Left histograms are data and right ones are Monte-Carlo.

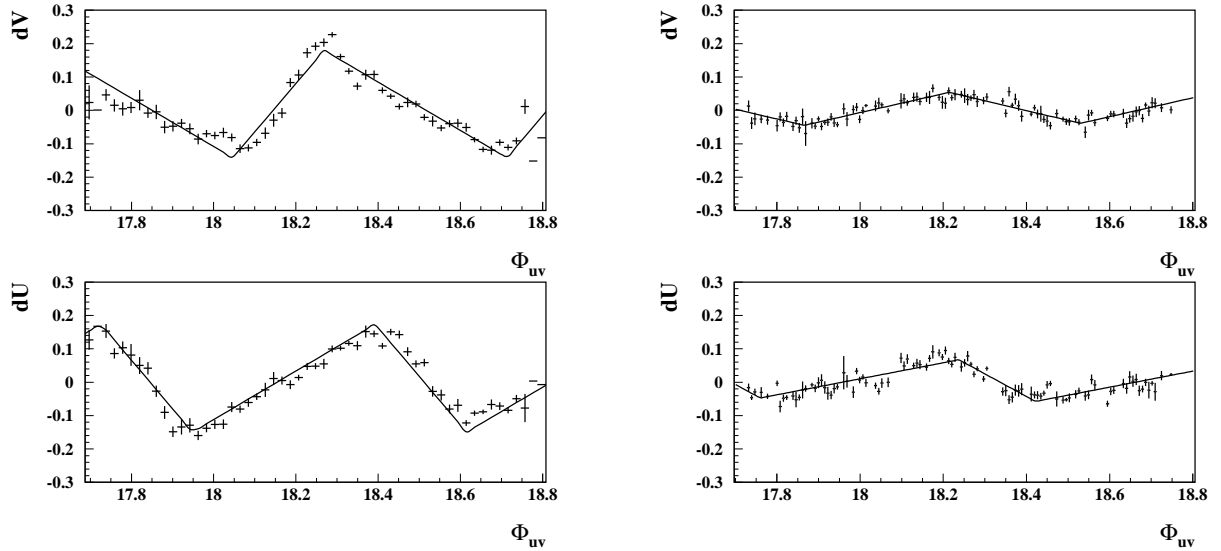


Figure 16:  $w - w_{beam}$  vs  $\phi_{uv}$  ( $w=u$  or  $v$ ) after correction of the function of figure 15 (points with error bars).  $\phi_{uv}$  is given here in cell units of the middle sampling. Left histograms are data and right ones are Monte-Carlo.

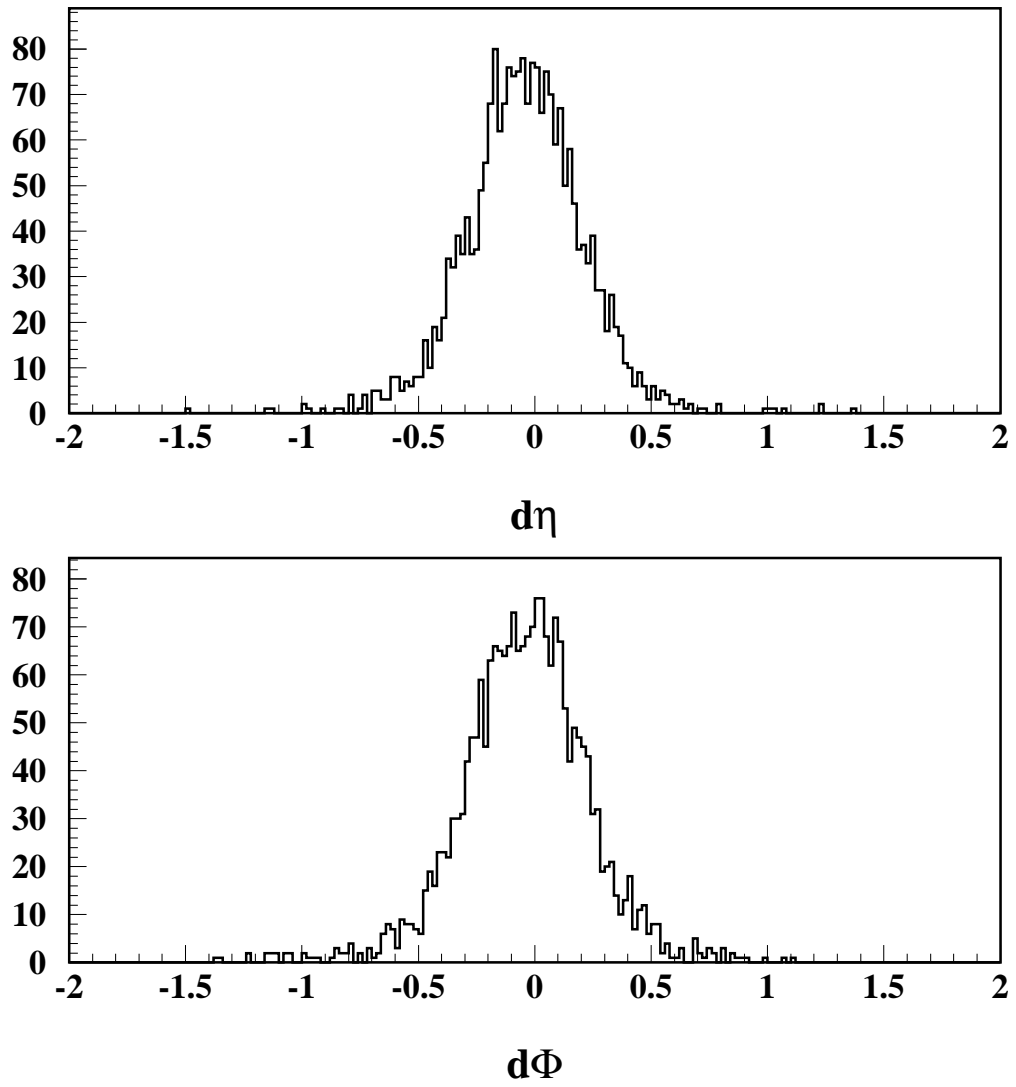


Figure 17: Distribution of  $d\eta$  and  $d\phi$  in mrad for electrons of 200 GeV.

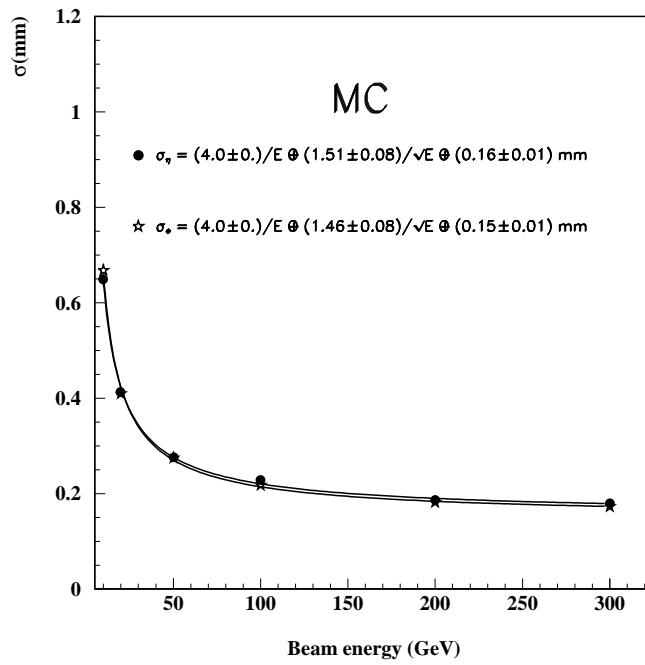
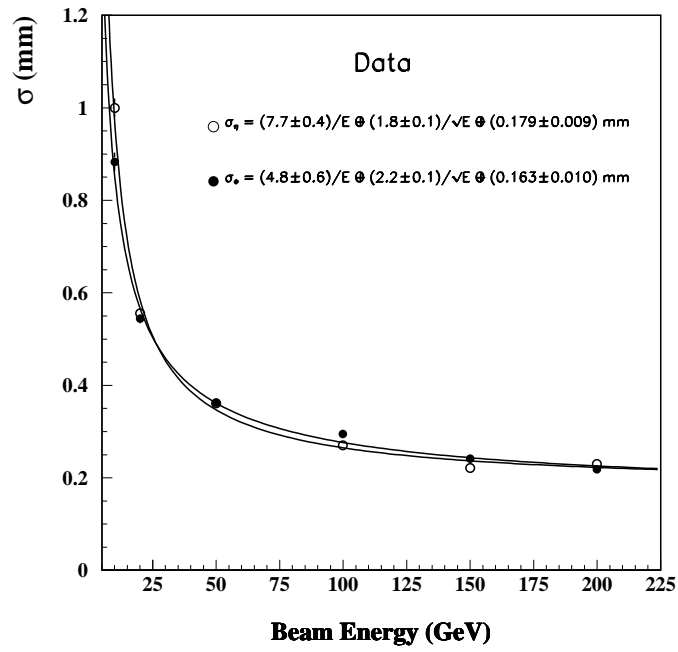


Figure 18: Position resolution for sampling UV

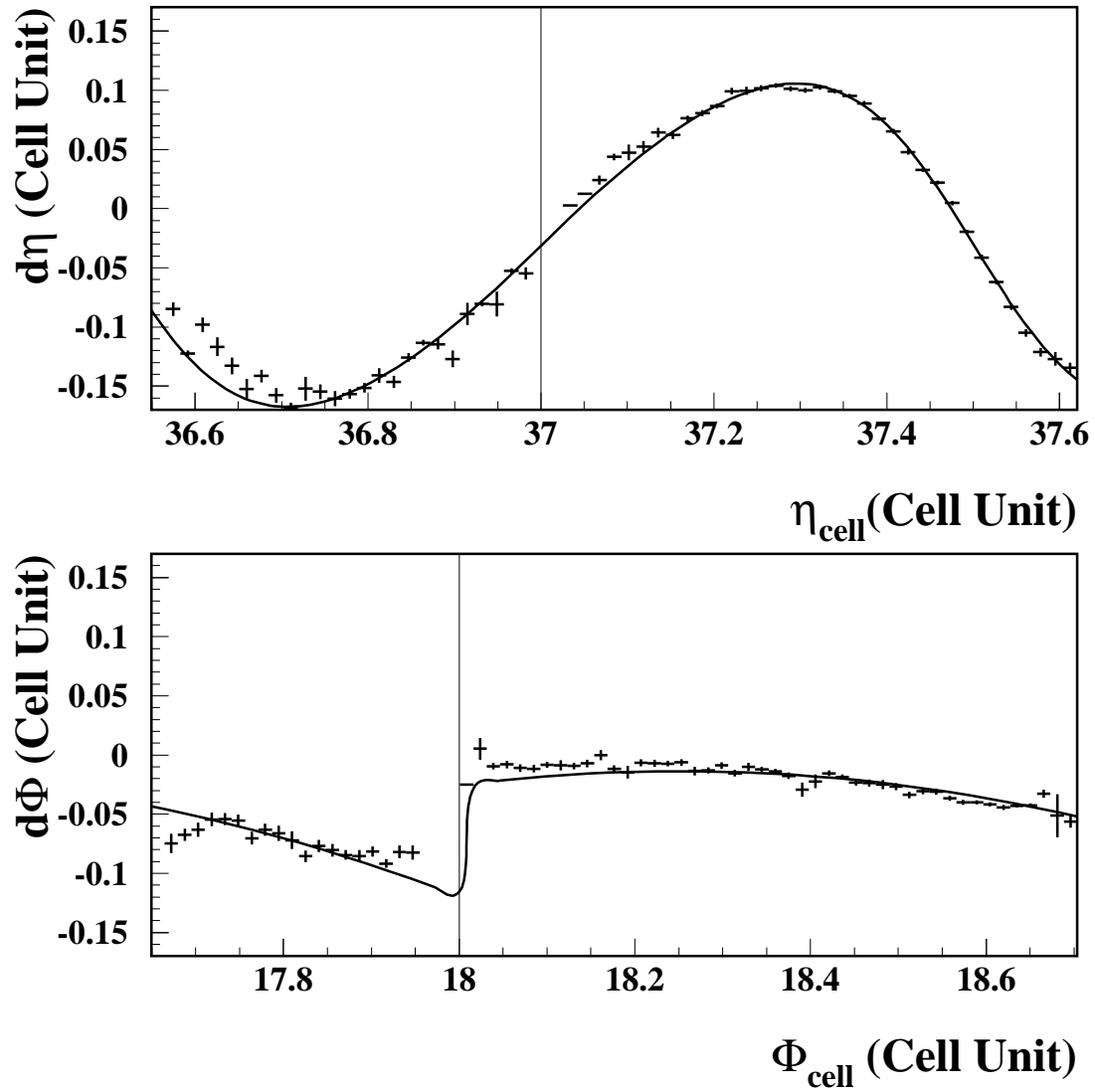


Figure 19:  $d\eta$  vs  $\eta_{\text{mid}}$  before any correction (crosses); the correction function is shown with a full line(see text).  $d\phi$  vs  $\phi_{\text{mid}}$  before any correction (crosses) ; the correction function is shown with a full line(see text). The vertical lines show the cell edges.

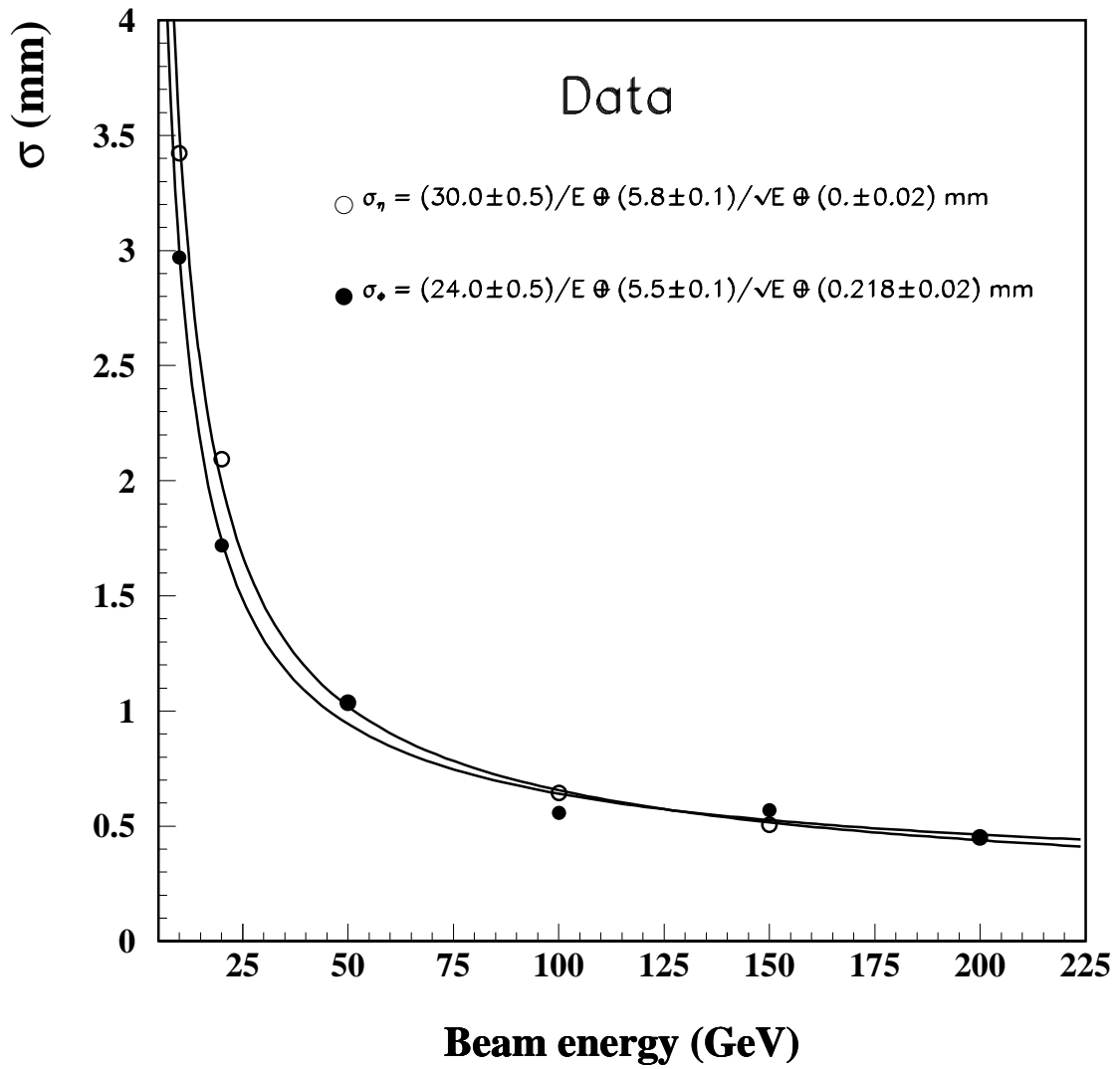


Figure 20: Resolution in position for the middle sampling after all corrections.



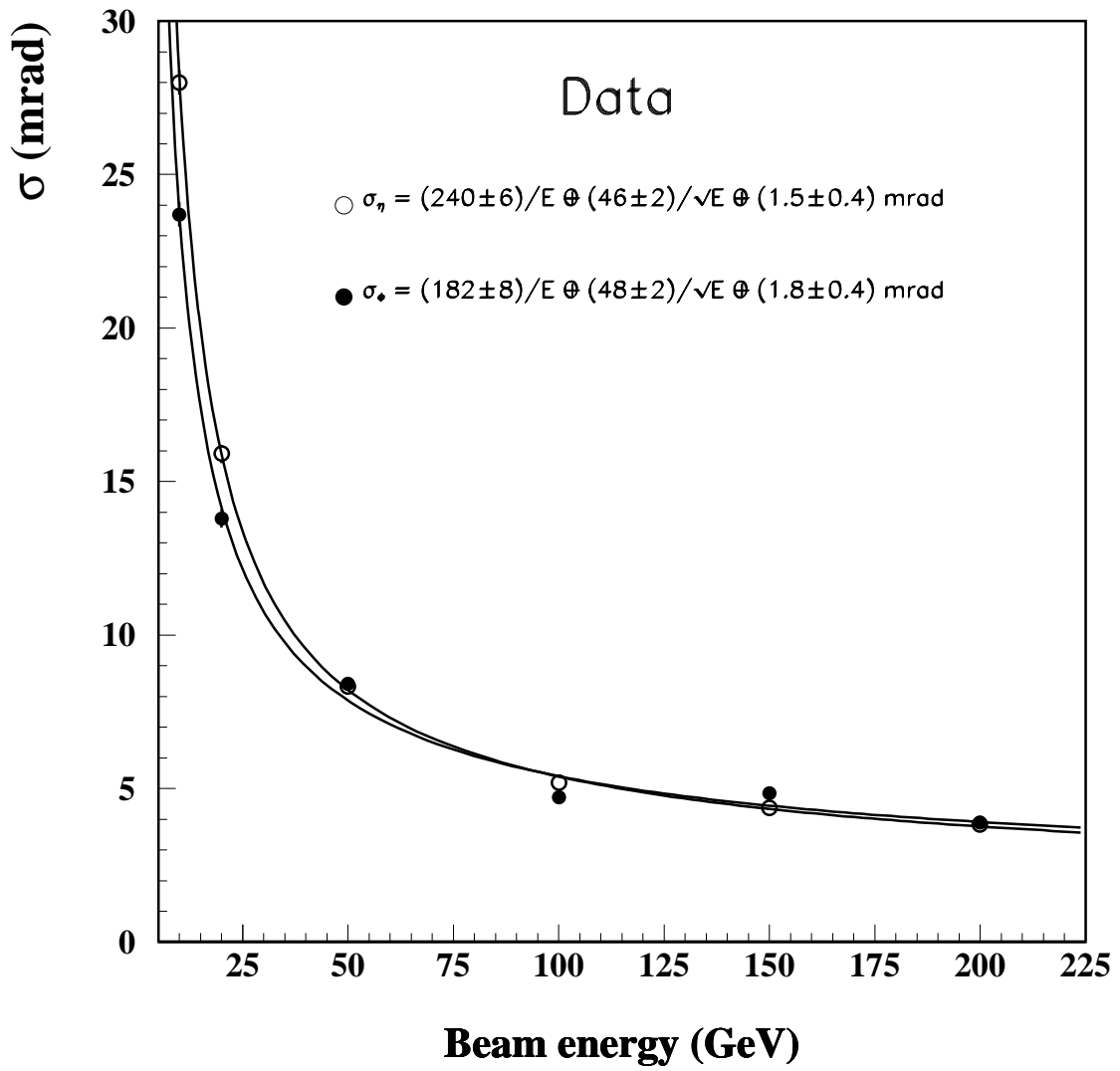


Figure 21: Angular resolution obtained by the UV preshower and the middle sampling of the electromagnetic calorimeter.

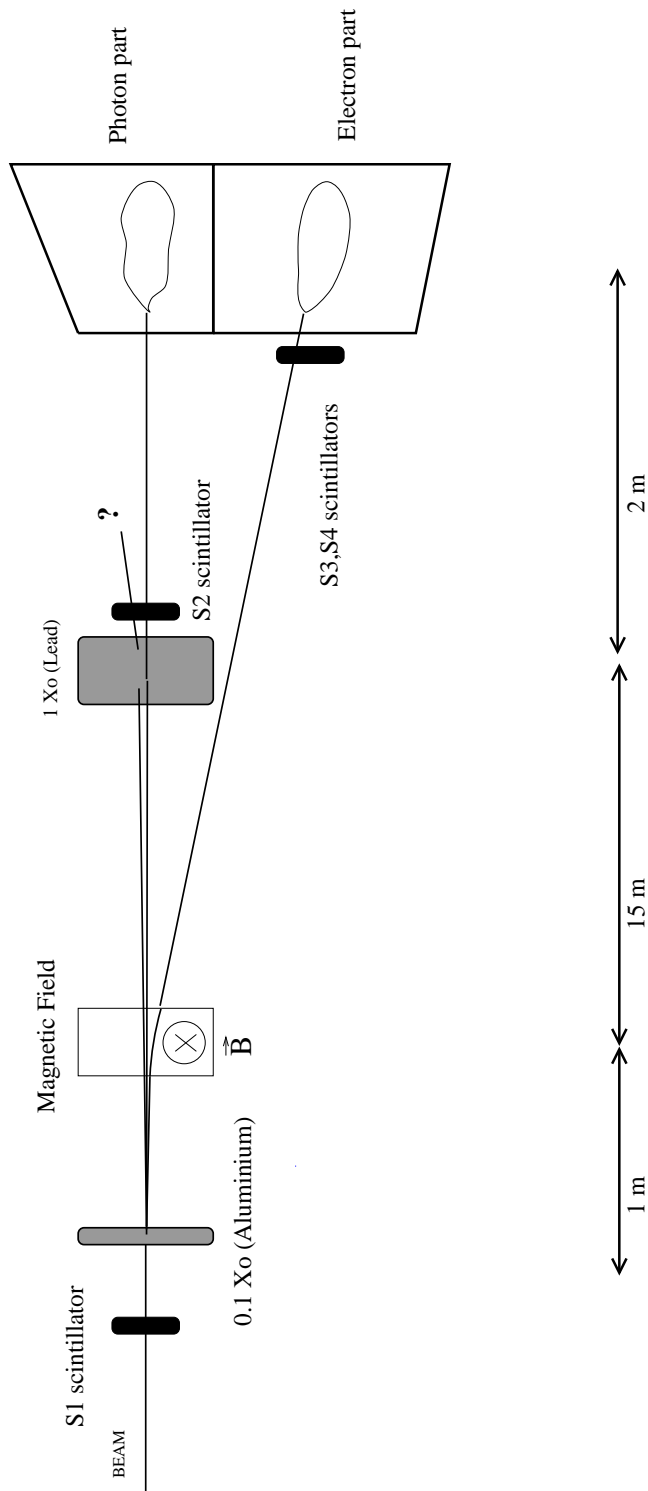


Figure 22: Testbeam setup for photons (not at scale)

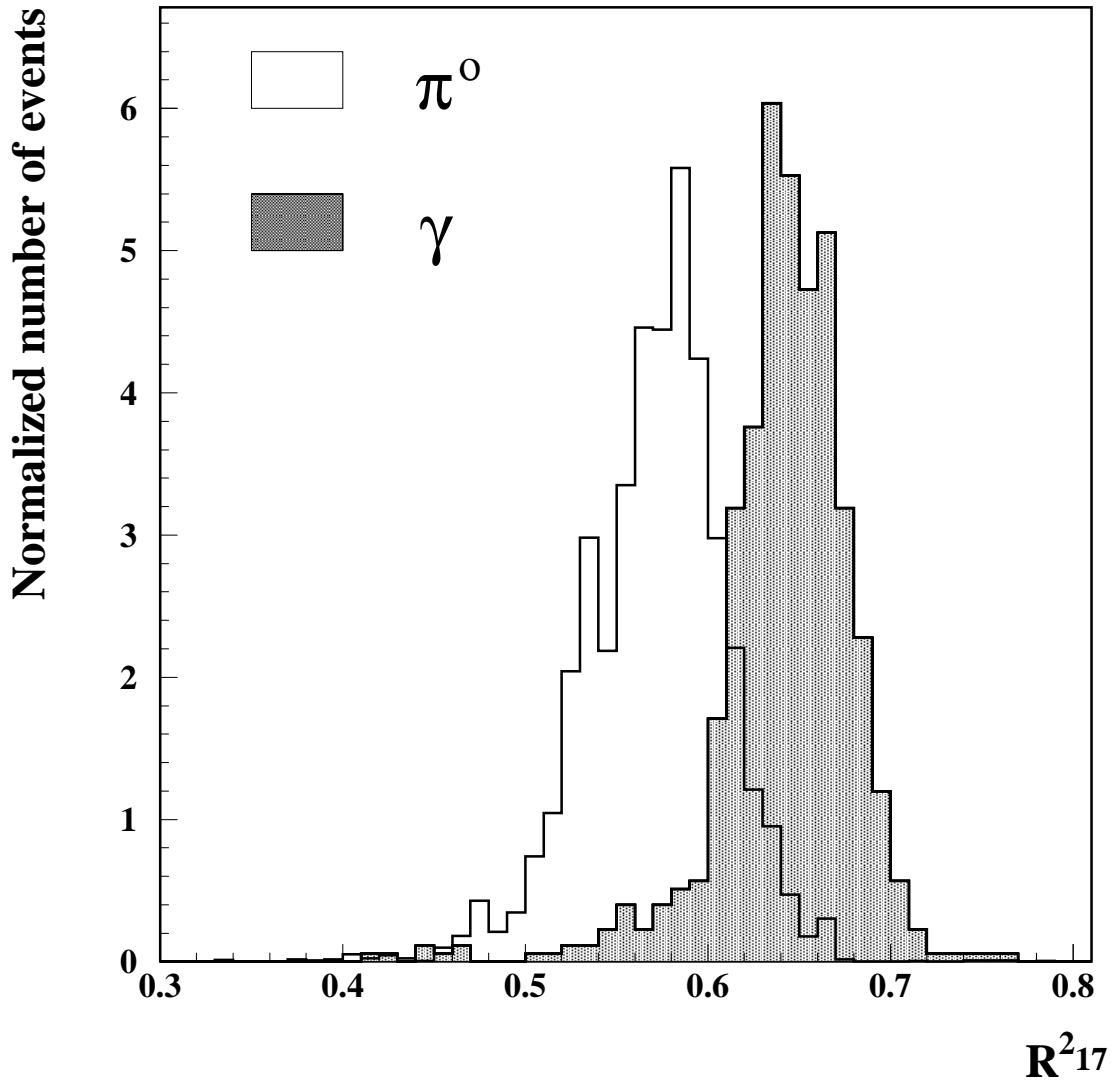


Figure 23: Distribution of dispersion ratio ( $R^2_{17}$ ) for  $\gamma$  and  $\pi^0$  of  $E_t=50$  GeV and at  $\eta=0.67$

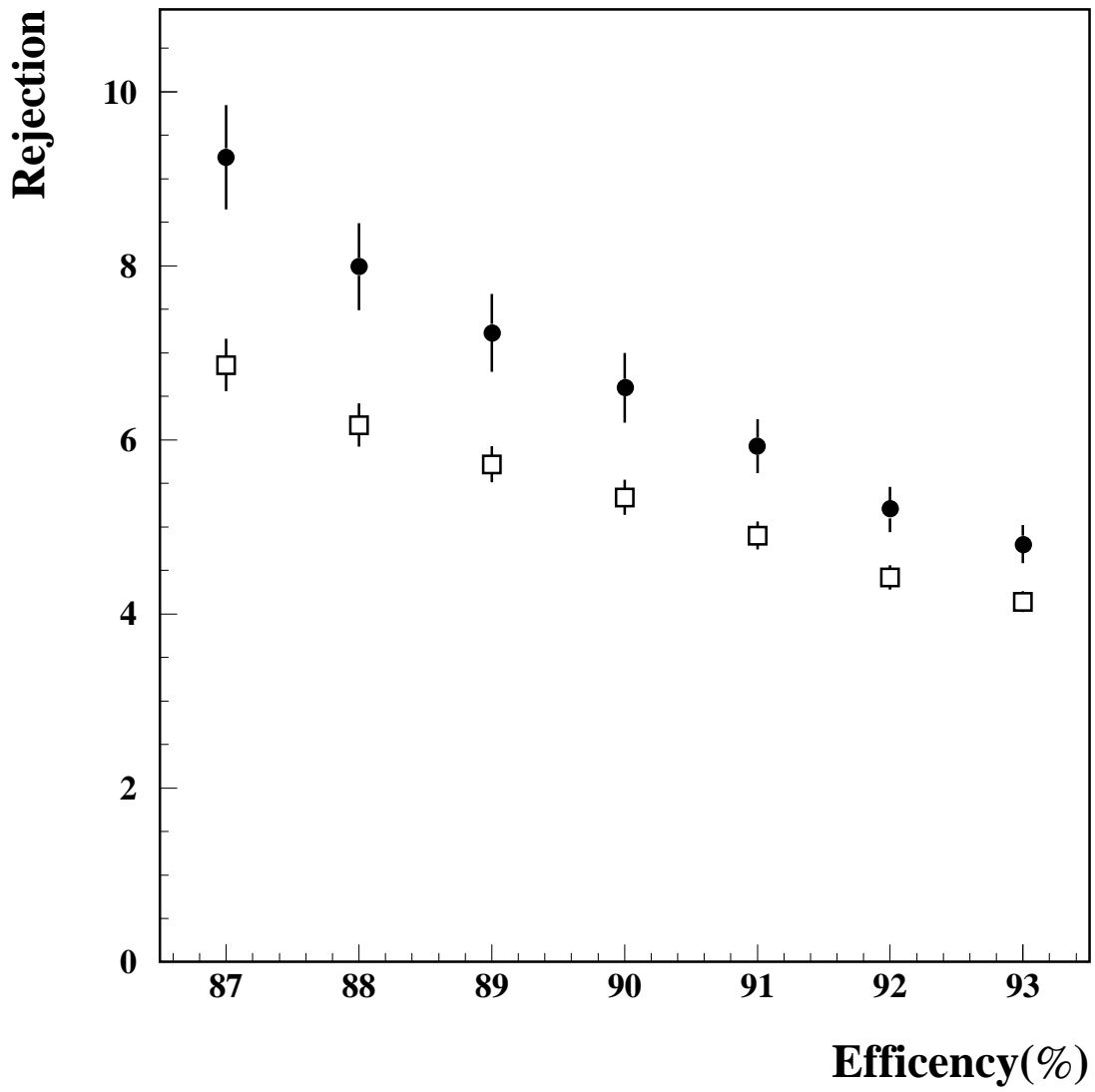


Figure 24: Rejection of  $\pi^0$  versus  $\gamma$  efficiency with the optimistic method (circle) or the conservative one (box)